Title
Detection of waves in the Earth’s outer core using geomagnetic data-driven techniques

Author
Chi Duran, Rodrigo Kimyen

Publication Date
2023

Peer reviewed|Thesis/dissertation

Detection of waves in the Earth's outer core using geomagnetic data-driven techniques

by

Rodrigo Chi Durán

A dissertation submitted in partial satisfaction of the

requirements for the degree of

Doctor of Philosophy

in

Earth and Planetary Science

in the

Graduate Division

of the

University of California, Berkeley

Committee in charge:

Professor Bruce Buffett, Chair
Professor Douglas Dreger
Professor Alexis Kaminski

Summer 2023

Detection of waves in the Earth's outer core using geomagnetic data-driven techniques

Abstract

Detection of waves in the Earth's outer core using geomagnetic data-driven techniques

by

Rodrigo Chi Durán

Doctor of Philosophy in Earth and Planetary Science

University of California, Berkeley

Professor Bruce Buffett, Chair

Short-period fluctuations in the Earth's geomagnetic field have been observed through satellite observations over the past 20 years. In this work, we explore the use of two data driven-techniques to quantify and interpret the short-period fluctuations. Complex empirical orthogonal functions (CEOFs) are applied to observations of the second time derivative of the geomagnetic field (secular acceleration) from several localized regions of the CHAOS6 model (Finlay et al., 2016). We found evidence of eastward and westward traveling waves with periods of 7.08 $\pm$ 0.58 and 15.73 $\pm$ 4.44 years, respectively, in the Atlantic and South Asia regions. Furthermore, we have applied dynamic mode decomposition (DMD) to investigate the temporal evolution of the radial magnetic field (Br) and secular variation (SV) at high latitudes using CHAOS7 (Finlay et al., 2020). Our results exhibit waves with periods of 19.1 and 58.4 years. A 60-year wave is compatible with prior predictions for zonal waves in a stratified fluid. The 20-year wave is consistent with previous findings at high latitudes, although the wave characteristics do not permit a simple interpretation. Finally, we study positive and negative geomagnetic acceleration patches moving westward at high latitudes. Magnetic Rossby waves offer one possible interpretation of the observations. This type of waves can account for the propagation direction and phase velocity. However, the predicted spatial pattern of the magnetic field variation is more complex than the observations. Zonal MAC waves, however, can explain the observed field with a stratified layer at the core's top. In conclusion, these results are significant for comprehending the dynamics of the geomagnetic field and its impact on the Earth's outer core structure.

To everyone who loves what they do (and can make a living doing it)

Contents

List of Figures

List of Tables

Acknowledgments

The past five years of my Ph.D. journey in Berkeley have been a rollercoaster in the best possible way. There have been ups, downs, and countless memorable moments. As I sit to write this, I am flooded with gratitude for so many who have had my back. I genuinely hope I do not leave anyone out.

To begin with, I want to express my appreciation to my main advisor, Bruce Buffett, who has been extraordinarily supportive over these five years. His knack for navigating the right path, his unwavering support when I encountered challenges, and his incredible ability to keep me motivated have been vital to my progress. Thank you, Bruce, for these amazing years of working together; I learned so much from you.

I would also like to thank my second advisor, Douglas Dreger. Even though our work is not included in this dissertation, the knowledge I gained under his supervision has proven invaluable. His constant feedback and advice have served as essential lessons, influencing my academic journey and providing insights into life beyond academia.

I want to thank my qualifying exam and dissertation committee members: Alexis Kaminski, Michael Manga, Phillips Marcus, and Harriet Lau. In particular, I thank Prof. Kaminski for joining my dissertation committee at the last minute; your feedback has been essential for this thesis.

I would like to acknowledge the former and current members of Buffett's group: Will Davis, Nicholas Knezek, Maggie Avery, Tushar Mittal, Daria Holdenried-Chernoff, Sebastian Glane, and Hiro Matsui for their support. Additionally, my gratitude extends to my external collaborators, Avinash Nayak and Artie Rodgers.

To my EPS colleagues and friends, this journey would not have been as enjoyable without you: Andy Tholt, Claire Doody, Mara Reed, Erin Redwing, Dani Lindsay, Jiwoon Hwang, Quentin Nicolas, Susan Mullen, Andrew Turner, Sarina Patel, Sevan Adourian, Tyler Cadena, and Chris Moeckel. I also want to acknowledge my Berkeley friends, Leah Jaffe, Ignacio Benavente, Edgar Sanchez, and Piero Zanoco, with whom I shared great times at different points during this long journey. Thank you all for your friendship and support, and for making this experience joyful and unforgettable.

I truly owe everything to my family back in Chile. My dad, mom, brother, and the entire family consistently checked in on me while I was kilometers away. A deep thanks to my partner, Marcela, for your companionship and love, especially as this journey drew to a close. I am looking forward to the moment when we can be together—and hopefully, that moment will last forever!

Lastly, a massive thanks to Fulbright Chile and ANID for granting me the scholarship opportunity to study in the US. Without them, I would not be here, tackling this dissertation in English or experiencing the great number of cultural moments that have deeply shaped me.

Chapter 1

Introduction

The geomagnetic field observed above the Earth's surface originates from multiple sources, both internal and external to the planet. These sources include the core, lithosphere, ionosphere, and magnetosphere (see Figure 1.1). The dominant dipole component of the magnetic field is generated by internal sources. Fluid motions in the liquid metal outer core generate the internal field through a process known as the geodynamo. The Earth's rotation strongly influences the movement of liquid metal, creating electric currents that continually regenerate the magnetic field. Crustal rocks contribute to the magnetic field through the presence of magnetized rocks and minerals. Electric currents in the weakly conducting mantle and ocean can also contribute to the magnetic field above the surface. External sources such as the ionosphere and magnetosphere also play a role. The ionosphere is a layer of the Earth's atmosphere ionized by solar radiation. The interaction between charged particles in the ionosphere and the Earth's magnetic field causes changes and fluctuations in the field. The magnetosphere is a region in space where the Earth's magnetic field dominates over the solar wind which contributes to the complexity and dynamics of the field.

This study addresses the core-generated field and its time variation in order to investigate the dynamics of the Earth's interior. Changes over millennial timescales and longer can be reconstructed using paleomagnetic data (Constable & Johnson, 2005), although reconstructions of the field variations have relatively few spatial details. Historical and satellite magnetic observations provide greater spatial detail on timescales of a few years to a few hundred years (e.g. Matzka et al., 2010). Shorter period fluctuations likely exist in the core due to inertial waves and other dynamics associated with the rapidly rotating, low-viscosity fluid core (Lesur et al., 2022). However, our ability to detect these short-period fluctuations is limited by the low amplitude of the magnetic fluctuations (Gillet et al., 2022) and by the screening effects of the Earth's conductive mantle (Lesur et al., 2022).

Models for the geomagnetic field over the last 20 years incorporate data from both satellites and ground observatories. Satellite observations are particularly important because they provide much finer spatial sampling and permit greater separation of the internal and exte-

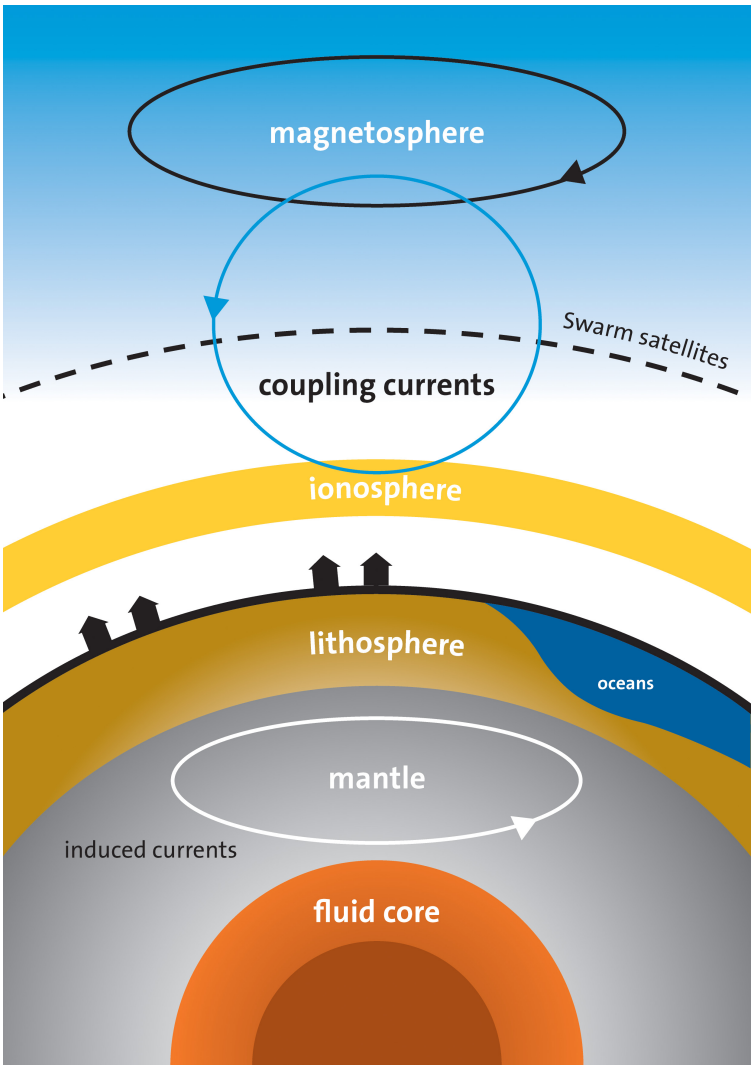

Figure 1.1: The figure displays various sources that contribute to the magnetic field measured by satellite missions (in this particular case, European Swarm missions) which include the core, mantle, lithosphere, ionosphere, and magnetosphere. The coupling currents, also known as field-aligned currents, flow along magnetic field lines between the magnetosphere and ionosphere. Figure made by ESA/DTU Space.

rior magnetic fields. This allow for more precise characterizations of the internal magnetic field (B), as well as the first and second derivatives of the field, known as the geomagnetic secular variation (SV) and secular acceleration (SA), respectively (Finlay et al., 2016). A large fraction of the SV can be explained using a slowly evolving flow due to convection in the core. Shorter period dynamics are more readily detected in the SA because we expect

the large convective flow to have a much smaller contribution. Short-period fluctuations in the geomagnetic acceleration are particularly useful for studying fluid motion in the Earth's core, whereas waves are harder to detect in the first derivative due to the strong influence of quasi-steady flow in the outer core.

Since the observed geomagnetic acceleration is likely a superposition of many different wave components, methods for decomposing the signal into individual waveforms are essential. Recent advances in data-driven techniques offer several suitable tools for coping with this challenge. A common elements of these approaches is that they do not rely on a priori assumptions about the data or the underlying processes. This makes them flexible and adaptive, allowing them to be applied to a wide range of signals and datasets. In this thesis, we apply two data-driven methods; one is called Complex Empirical Orthogonal Functions (CEOF) and the other is called Dynamic Mode Decomposition (DMD). CEOF is an extension of the Empirical Orthogonal Function (EOF) method, which allows for the decomposition of a signal into complex-valued modes. This enables the identification of oscillatory patterns, including amplitude and phase information, which are particularly useful for analyzing periodic signals and traveling waves. Similar information can be obtained from the DMD technique, which can be applied to capture complex and nonlinear dynamics in the data. This approach decomposes the signal into a set of spatial modes and their associated temporal behaviors, allowing for the identification of both linear and nonlinear patterns in the data. DMD and CEOF are effective for decomposing geomagnetic signals because they provide time-frequency representations, capture nonlinear dynamics, decompose into complex-valued modes, offer reduced-order representations, and have broad applicability across various fields.

This thesis aims to identify core waves in geomagnetic data using data-driven techniques. We begin in Chapter 2 with a brief review of basic concepts in geomagnetism. In Chapter 3, the application of CEOF to local regions on Earth is examined to identify distinct wave features. Chapter 4 investigates the SA pulses located at high latitudes, comparing them with forward models derived from MAC Waves and Magnetic Rossby Waves. In Chapter 5, the application of DMD to geomagnetic data from the North Pole is presented, revealing modes that are consistent with MAC wave models. Finally, Chapter 6 provides a summary of this work and offers an outlook on future research directions in this field.

Chapter 2

Background

This chapter aims to provide a concise overview of the concepts that will be further developed in subsequent chapters. The majority of the information presented here has been extracted from the works of Jackson and Finlay (2015), Finlay (2019), Lesur et al. (2022), and Gillet et al. (2022). More in-depth and extensive exploration of the topics can be found in the aforementioned publications.

2.1 Geomagnetic Observations

The investigation of Earth's magnetic field boasts an extensive chronology, potentially tracing back to the 12th century when the Chinese initially utilized it for navigational purposes. In 1600, Gilbert proposed the groundbreaking hypothesis that Earth functions as a colossal magnet. Nevertheless, the origins of Earth's magnetic field persisted as an enigma for an additional three centuries. From early on, it was recognized that the field's characteristics were not immutable, with the secular variation being meticulously documented. Consequently, a valuable historical archive of fluctuations in intensity and, specifically, orientation, has been established for research purposes.

Observations from various sources over the last century allow for a direct assessment of the present-day magnetic field at the Earth's surface. It is customary to separate the surface magnetic field into an internal field due to electric currents in the core and an external field due to electric currents above the surface. The main data sources include ground-based observatories and measurements from satellite missions such as Swarm, CHAMP, and Ørsted. The satellite measurements, in particular, have profoundly improved our ability to characterize the geomagnetic field. We typically assume that the surface magnetic field can be represented as a potential field. Both the internal and external fields are expressed in the form of spherical harmonic expansion, where the coefficients of the expansion are known as Gauss coefficients. The internal magnetic field is usually truncated at degree $l = 14$ because the higher degrees are obscured by the crustal magnetization (Olsen et al., 2006).

Ground Magnetic Observatories

Ground Magnetic Observatories are facilities that measure the Earth's magnetic field at specific locations on the Earth's surface. These observatories are important for monitoring the evolution of the Earth's main magnetic field, which originates in the fluid outer core. The data collected from these observatories are used to study changes in the Earth's magnetic field over time, which can provide insights into the dynamics of the Earth's interior. To investigate changes in the Earth's core field over durations ranging from years to decades, researchers usually either examine magnetic changes recorded at specific locations or analyze spherical harmonic field models. Although ground stations provide excellent temporal resolution, their uneven spatial distribution makes global studies of core field changes difficult (see Figure 2.1). On the other hand, constructing field models requires prior information to address the non-uniqueness of the geomagnetic inverse problem.

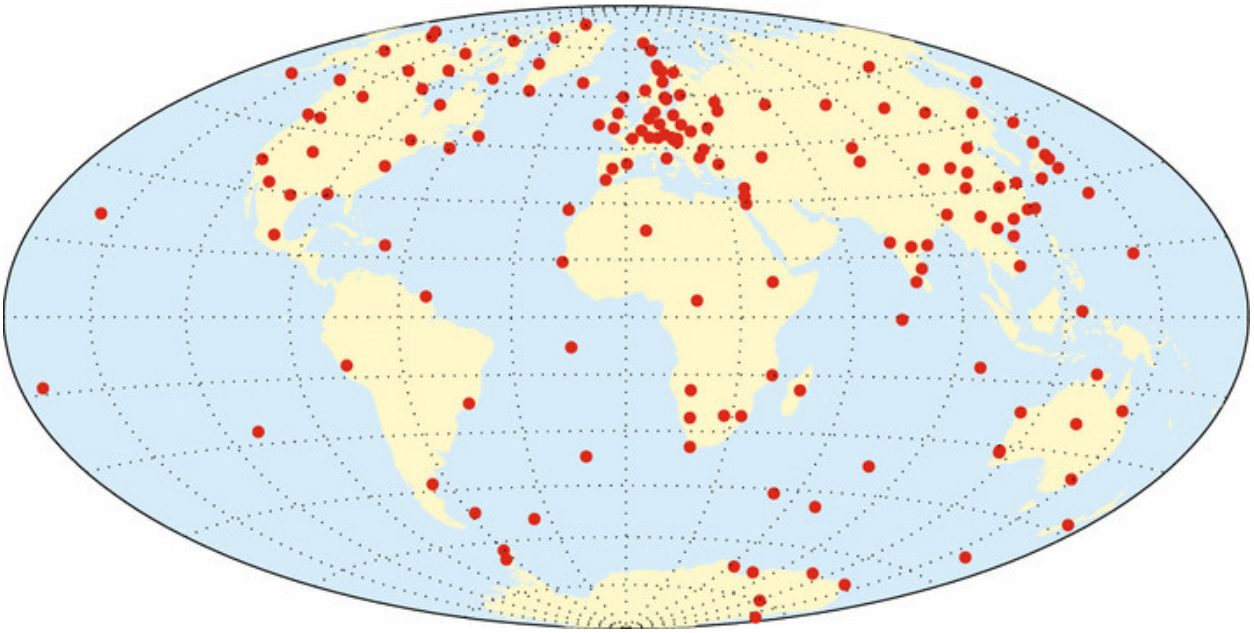

Figure 2.1: Geomagnetic Observatories included in CHAOS-6 model. Figure extracted from Finlay et al. (2016)

Satellite Missions

The advent of magnetic field measurements from low Earth-orbiting satellites has facilitated the mapping of smaller spatial structures in the core field changes, owing to the nearly comprehensive global coverage. The continuous space records spanning the last two decades have granted valuable perspectives on the magnetic field's spatial and temporal variations. Specif-

ically, measurements from the Danish Ørsted satellite (1999-2014), the German CHAMP satellite (2000-2010), and the European Swarm satellite trio mission (2013-present) have significantly enhanced the constraints derived from geomagnetic data (Domingos et al., 2019; Olsen & Stolle, 2012). Additionally, calibrated CryoSat-2 satellite measurements (2010-present) contribute further constraints on field variations, particularly during the 2010-2014 temporal gap between CHAMP and Swarm (Olsen et al., 2020). Although the primary physical mechanisms driving most field changes operate on time scales exceeding the satellite era (i.e., the past 20 years), satellite data alone may be employed to characterize shorter inter-annual fluctuations. See Table 2.1 for more information about these missions.

Table 2.1: Comparison of Satellite Missions

	Ørsted	**CHAMP**	**Swarm**
Launch Date	1999	2000	2013
Purpose	Measure Earth's magnetic field	Measure Earth's magnetic field and gravitational field	Provide high-precision measurements of magnetic signals from Earth's core, mantle, crust, oceans, ionosphere, and magnetosphere
Instruments	Magnetic field sensors, star imager	Magnetometers, accelerometers, GPS receiver, star sensors	Vector Field Magnetometer, Absolute Scalar Magnetometer, Startrackers, GPS receiver
Lifespan	1999-2014	2000-2010	Ongoing as of 2023 (originally 4 years planned)

2.2 Geomagnetic Field Modelling

To provide a quantitative depiction of the geomagnetic field, a suitable mathematical representation is required. This depiction can be accomplished through the use of potential theory, as first introduced by Gauss in 1838. In the absence of electric currents, Maxwell's equations require

$$\nabla \times \mathbf{B} = 0 \tag{2.1}$$

$$\nabla \cdot \mathbf{B} = 0 \tag{2.2}$$

Given equation 2.1, there is a scalar function V which satisfies

$$\mathbf{B} = -\nabla V \tag{2.3}$$

Using Equations 2.2 and 2.3 we obtain

$$\nabla^2 V = 0 \tag{2.4}$$

The geomagnetic potential V is customarily described in spherical coordinates (r, ϕ, θ), where θ is the colatitude, ϕ is the longitude, r is in the radial distance from the center of the Earth. Each component of the magnetic field can be written as

$$B_r = -\frac{\partial V}{\partial r} \tag{2.5}$$

$$B_\theta = -\frac{1}{r}\frac{\partial V}{\partial \theta} \tag{2.6}$$

$$B_\phi = -\frac{1}{r\sin\theta}\frac{\partial V}{\partial \phi} \tag{2.7}$$

The potential is commonly separated into a contribution from internal currents and a contribution from currents in space, relating to the field within and outside the core. The potential V_{int} due to internal currents can be expressed as a spherical harmonic expansion (Backus et al., 1996)

$$V_{\text{int}}(r, \theta, \phi, t) = a \sum_{\ell=1}^{\infty} \sum_{m=0}^{\ell} \left(\frac{a}{r}\right)^{\ell+1} P_\ell^m(\theta) \left[g_\ell^m(t) \cos m\phi + h_\ell^m(t) \sin m\phi\right] \tag{2.8}$$

where $P_\ell^m(\theta)$ is the Schmidt normalized Legendre function with degree ℓ and order m, and a is the radius of the Earth. In this expansion, the terms g_ℓ^m and h_ℓ^m are called the Gauss coefficients. These values represent the strength of magnetic sources inside and near the Earth, and they are determined by analyzing measurements of the magnetic field.

In order to construct accurate models of the Earth's main magnetic field, it is essential to account not only for its spatial dependence, but also for its slow temporal or secular variation. Traditional models, such as the International Geomagnetic Reference Field (IGRF), achieve this by employing linear interpolation between Gauss coefficients which are defined at reference epochs. However, more sophisticated models often utilize B-spline basis functions of order K (Bloxham & Jackson, 1992; De Boor, 1978) to represent the time dependence of the field. These functions allow for greater flexibility in capturing the complexities of the field's behavior over time, and have proven to be highly effective in producing more accurate models.

$$g_n^m(t) = \sum_p g_n^{m,p} \mathscr{B}_{K,p}(t) \tag{2.9}$$

where $g_n^{m,p}$ are a set of spline coefficients for each Gauss coefficient g_{mn}, defined at knots p that span the time interval of interest. The B-spline basis functions $\mathscr{B}_{K,p}$ are piecewise polynomials of order K (see example in Figure 2.2). The latest versions of advanced geomagnetic models, such as those in the CHAOS series, use B-splines of order 6. This allows the models to be differentiated twice with respect to time, making it easier to study field acceleration.

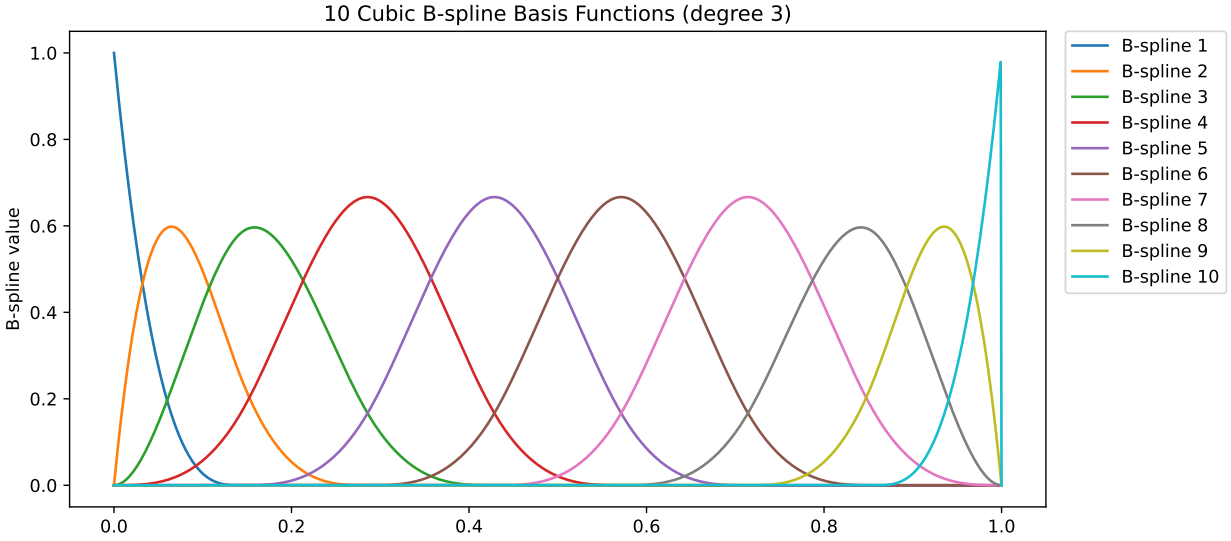

Figure 2.2: Temporal behavior of Gauss coefficients in internal field models can be effectively captured through a collection of 10 cubic B-spline basis functions. These basis functions possess localized ranges and can be combined with different weights to achieve the desired representation.

2.3 Geomagnectic Models

A number of global magnetic field models have been created using high-resolution satellite magnetic field data. The Ørsted Initial Field Model (OIFM) was the first global magnetic field model, published by Olsen et al. (2000), which provided a description of the magnetic field up to degree 19. However, the OIFM only reported the constant geomagnetic field and core secular variation at specific moments in time. Subsequent studies have improved upon this model by incorporating additional observations as they became available and implementing advancements in data assimilation and modeling techniques.

This thesis explores two distinct models that utilize ground-based and satellite data as "observations" to recover core dynamics. The first model, CHAOS-7 (Finlay et al., 2020), centers on the satellite era from 1998 to 2021 and integrates data from Oersted, SAC-C,

CHAMP, CryoSat-2, and Swarm missions. The model estimates the core field, projected onto splines, jointly with static crustal field models, low-degree magnetospheric field models, and the induced response in the mantle, subject to a mantle conductivity model. However, the ionospheric field contribution is not co-estimated, and CHAOS-7, constructed using adjusted regularizations, lacks associated uncertainties.

The second model, COV-OBS-x2 (Huder et al., 2020), spans the entire observatory era since 1840 and incorporates satellite data through virtual observatories (Hammer et al., 2021). The model co-estimates the core evolution with the magnetospheric external dipole in dipole coordinates, which is also projected onto splines but with a longer (2-year) knot spacing to accommodate periods with varying data coverage. However, this compromise precludes the description of fluctuations with periods shorter than approximately three years (Pick et al., 2019). The a priori information used to address the non-uniqueness of the inverse problem is based on stochastic processes that are compatible with the field's temporal spectrum, allowing for the extraction of realistic model uncertainties from the posterior covariance matrix.

2.4 The Geodynamo

Over the centuries, numerous mechanisms have been proposed to explain the origin of the Earth's magnetic field. However, current consensus holds that the core field is generated by the rapid and complex flow of highly conductive, metallic iron in the outer core. The fundamental concept underlying the geodynamo involves the expeditious movement of a portion of the fluid within an existing magnetic field. This motion generates an electric current that induces a secondary magnetic field, which is predominantly conveyed within the fluid flow ("frozen flux"). This secondary field augments the primary magnetic field. As the inner core progressively solidifies, an excess of lighter constituents is released at the boundary between the inner and outer core. This process gives rise to buoyancy, which in turn drives compositional convection within the outer core. The interplay between convection and Earth's rotation culminates in the intricate motion required for self-sustained dynamo activity.

Using Maxwell's equations and the momentum equation, the induction equation can be obtained as

$$\frac{\partial \mathbf{B}}{\partial t} = \nabla \times (\mathbf{u} \times \mathbf{B}) + \nabla \times (\eta \nabla \times \mathbf{B}), \tag{2.10}$$

where η is the magnetic diffusivity. The magnetic induction equation is supplemented by the solenoidal condition

$$\nabla \cdot \mathbf{B} = 0, \tag{2.11}$$

When η is treated as a constant the induction equation simplifies

$$\frac{\partial \mathbf{B}}{\partial t} = \nabla \times (\mathbf{u} \times \mathbf{B}) + \eta \nabla^2 \mathbf{B}, \tag{2.12}$$

where ∇^2 is the Laplacian operator. The first term on the right-hand side represents the induction of the magnetic field by the fluid flow. This term is responsible for the generation and maintenance of the magnetic field through the motion of the electrically conducting fluid. The second term represents the diffusion of the magnetic field. This term describes the decay of the magnetic field due to the finite electrical conductivity of the fluid. The diffusion term is often neglected on short timescales, so the induction equation reduces to

$$\frac{\partial \mathbf{B}}{\partial t} = \nabla \times (\mathbf{u} \times \mathbf{B}). \tag{2.13}$$

Most studies focus on the radial component of the magnetic field due to the discontinuity of the tangential components of the magnetic field at the core-mantle boundary. In comparison, the radial component of the field is expected to be continuous (R. Holme, 2007). The induction equation for the radial component B_r at the core-mantle boundary becomes

$$\frac{\partial B_r}{\partial t} = -\mathbf{u}_H \cdot \nabla_H B_r - B_r(\nabla_H \cdot \mathbf{u}_H) \tag{2.14}$$

where ∇_H is the horizontal gradient operator and u_H is the horizontal component of the velocity. (The radial component of the velocity vanishes at the core-mantle boundary). The first term represent the advection of radial magnetic field by u_H; the second term accounts for the change in B_r due to horizontal divergence of U_H.

The second derivative of the magnetic field's radial component can be written as

$$\frac{\partial^2 B_r}{\partial t^2} = -\dot{\mathbf{u}}_H \cdot \nabla_H B_r - \mathbf{u}_H \cdot \nabla_H \dot{B}_r - \dot{B}_r(\nabla_H \cdot \mathbf{u}_H) - B_r(\nabla_H \cdot \dot{\mathbf{u}}_H), \tag{2.15}$$

Terms involving the time derivative of the radial magnetic field, $\dot{B}_r$, are small compared the terms involving $\dot{u}_H$. This is why a steady flow contributes very little to the secular acceleration. By comparison, wave motion with a fluid acceleration has a more prominent role in the second time derivative of B_r.

2.5 Magnetic Waves

Investigations into secular acceleration reveal a more complex dynamic from decadal to centennial timescales (Finlay et al., 2020). The underlying causes of these fluctuations remain unclear, although various evidence gathered from geodynamo models suggests the involvement of hydromagnetic waves within the Earth's core (Aubert & Gillet, 2021).

Within the Earth's core, rotation and inertia serve as restoring forces that facilitate the propagation of inertial waves. One such wave is a Rossby wave, which is analogous to Rossby waves in the atmosphere; they propagate in the core with a period of a few weeks. Another type of wave that can propagate within the Earth's core relies on the magnetic field as a restoring force. These magnetohydrodynamic waves were first derived by Alfvén

(1943) and have since been identified in the Earth's magnetosphere and core, as well as in laboratory experiments (e.g. Braginsky, 1970). Other types of waves emerge when rotation and a magnetic field are combined as the restoring forces in the governing equations. For example, we recover Rossby waves that are slightly modified by the presence of a magnetic field. We also find slow waves (periods longer than 100 years) in which the rotation (Coriolis) and magnetic restoring forces nearly balance. These waves are sometimes called Magnetic-Coriolis (MC) waves (Lehnert, 1954). Some examples of MC waves in the Earth's core have been proposed by Hide (1966) and Gerick et al. (2021).

Fluid stratification is another restoring force that gives rise to additional types of waves. Waves with inter-annual periods and longer are possible in a stratified layer situated at the top of the Earth's core. The interplay between magnetic, Archimedes (buoyancy), and Coriolis forces produces waves known as MAC waves. These waves have been proposed to account for the intense non-zonal movements observed with inter-annual periods in the equatorial region. MAC waves also offer a description of zonal flow in the core with periods of several decades.
The influence of buoyancy in the stable layer is determined by the gradient of the density profile beneath the core-mantle boundary (CMB). We remove the influence of pressure induced changes in density by defining a reference density profile $\rho_0(r)$ for a well-mixed and adiabatic fluid. The relevant density profile for determining stratification is defined by $\rho'(r) = \rho(r) - \rho_0(r)$, where $\rho(r)$ is the total density profile inferred from seismology. The strength of fluid stratification is assessed through the Brunt–Vaïsala frequency,

$$N = \sqrt{-\frac{g}{\rho}\frac{d\rho'}{dr}} \tag{2.16}$$

where g denotes the gravitational acceleration. Several simplified representations of $N(r)$ are used in models for the waves. Sometimes the stratification is specified by a constant value of N and a layer thickness H (Braginsky, 1993; Braginsky, 1999). Other times the stratification is allowed to decrease linearly with the radius from a maximum value at the CMB. In this case, the stratification is defined by the values of N_{max} and H By adjusting N (or N_{max}) and H, it is feasible to align the periodicity of the waves with the periods of the SA pulses.

Chapter 3

Decomposition of geomagnetic secular acceleration into traveling waves using complex empirical orthogonal functions

This work has been previously published as: Chi-Durán, R., Avery, M. S.,Knezek, N., & Buffett, B. A. (2020). *Decomposition of geomagnetic secular acceleration into traveling waves using complex empirical orthogonal functions.* Geophysical Research Letters, 47, e2020GL087940. https://doi.org/10.1029/2020GL087940

Summary

Satellite observations reveal short pulses in the second time-derivative of the geomagnetic field. We seek to interpret these signals using complex empirical orthogonal functions (CEOFs). This methodology decomposes the signal into traveling waves, permitting estimates for the period, angular wave number and phase velocity. We recover CEOFs from the CHAOS-6 model, focusing on three geographic regions with strong secular acceleration. Two regions are confined to the equator, while the third is located under Alaska. We find evidence for both eastward and westward traveling waves with periods between 7 and 20 years. There is also evidence for weaker standing waves with complex spatial patterns. Two of the three regions have waves that are compatible with predictions for waves in a stratified fluid. Our results yield estimates for the structure of fluid stratification at the top of the core.

3.1 Introduction

The Earth's geomagnetic field is continually changing in time due to fluid motions and magnetic diffusion in the liquid metal core (e.g. Jackson & Finlay, 2015). These processes are

responsible for changes in the geomagnetic field over a vast range of timescales. Short-period fluctuations have been detected in satellite observations over the past 20 years (Friis-Christensen et al., 2006; Maus, 2007; Sabaka et al., 2015). Improved spatial coverage with satellite observations has also enhanced the fidelity of models for changes in the geomagnetic field (Finlay et al., 2016; Finlay et al., 2015; Olsen et al., 2014; Olsen et al., 2006; Olsen et al., 2009, 2010).

Most of the recent models for the geomagnetic field include data from satellites and ground observatories (Finlay et al., 2016). This data has enabled more accurate descriptions of the second time derivative in the geomagnetic field, sometimes called secular acceleration. The geomagnetic acceleration exhibits short-period fluctuations, which means that insights can be drawn using only data from the satellite era. We focus on short-period waves because the fluid motion is more easily detected in geomagnetic secular acceleration. By comparison, waves are difficult to detect in the first time derivative due to large contributions from quasi-steady flow in the outer core.

A variety of waves are predicted for the Earth's core, including Alfvén waves (Braginsky, 1970), inertial waves (Tilgner, 2015), MAC waves (Braginsky, 1993), eMAC waves (Buffett & Matsui, 2019) and magnetostrophic waves (Canet et al., 2014; Hori et al., 2015). The observed geomagnetic acceleration is likely a superposition of many different waves, so it is important to have methods for decomposing the signal into individual wave components. Empirical Orthogonal Functions (EOF) are commonly used to analyze variability in meteorological observations (Horel, 1984), although the method has recently been applied to the geomagnetic field (Pais et al., 2015). The standard methodology produces variability with a fixed spatial pattern, which restricts the utility of EOFs to standing waves. Extensions are required to analyze both traveling and standing waves. One extension, known as complex EOF (CEOF), is specifically designed to identify traveling waves. This approach has been applied with great success in a number of geophysical problems (Edwards & Seim, 2008; Horel, 1984; Susanto et al., 1998). It is also well suited for the analysis of geomagnetic acceleration. Once the traveling waves are extracted from the geophysical signal, it is possible to estimate the temporal period, the spatial wavenumber and the phase velocity of the wave components.

3.2 Complex Empirical Orthogonal Function

Decomposition of a geophysical signal using the Empirical Orthogonal Functions (EOFs) is a powerful technique for characterizing the dominant modes of variability. Normally, the variability is described with a fixed spatial pattern and a time-varying amplitude. An extension of the EOF methodology (known as complex EOF or CEOF) was first introduced to analyze oceanographic waves (Barnett, 1983), although the approach is easily adapted to the problem of waves in the Earth's core.

A clear explanation of this technique can be found in Esquivel and Messina (2008), so we give only a brief summary. Consider a scalar field $u(x_j, t_k)$, where x_j are the different positions ($j = 1, \ldots, M$) and t_k are the different times the signal is sampled ($k = 1, \ldots, N$). To recover the phase of a traveling wave we construct a complex data set by applying a Hilbert transform to u to define $\hat{u}$:

$$\hat{u}(x_j, t) = \frac{1}{\pi} \int_{-\infty}^{\infty} \frac{u(x_j, \tau)}{t - \tau} d\tau \,. \tag{3.1}$$

In practice the Hilbert transform is computed by shifting the phase of the Fourier transform of u by $\pi/2$ before applying an inverse transform back to the time domain. The new complex data set becomes

$$\tilde{u}(x_j, t_k) = u(x_j, t_k) + i\hat{u}(x_j, t_k) \,, \tag{3.2}$$

which is analyzed using the standard EOF methodology. We remove the time average, $\langle \tilde{u} \rangle$, from the data to define $X = (\tilde{u} - \langle \tilde{u} \rangle)^T$, where T is the transpose operator. Next, the covariance matrix C (a Hermitian $M \times M$ matrix) is defined as

$$C = \frac{1}{N} (X^*)^T X \,, \tag{3.3}$$

where the asterisk operator denotes the complex conjugate. The eigenvectors of C (denoted by φ_n for $n = 1, \ldots, M$) define the modes of variability; the corresponding eigenvalues λ_n are used to characterize the significance of each mode in explaining the data.

Given an eigenvector, φ_n, the time-dependent amplitude $A_n(t)$ of the corresponding mode can be determined by the projection of φ_n over the original (complex) data X. In other words, the amplitude of the n-th mode is given by

$$A_n(t_k) = \sum_{j=1}^{M} X(x_j, t_k) \varphi_n(x_j) \,. \tag{3.4}$$

The complex data set $X(x_j, t_k)$ is recovered by summing over all modes,

$$X(x_j, t_k) = \sum_{n=1}^{M} A_n(t_k) \varphi_n(x_j) \,. \tag{3.5}$$

The original geophysical signal $u(x_j, t_k)$ is obtained by taking the real part of X, so a single CEOF is defined by

$$\mathrm{CEOF}_n(x_j, t_k) = \mathrm{Re}\left[A_n(t_k) \varphi_n(x_j)\right] \tag{3.6}$$

Traveling waves can be represented by (6) because both A_n and φ_n are complex functions. To illustrate we note that the real part of the complex product $e^{i\omega t} e^{ikx}$ represents a traveling

wave, whereas the product of the real components (i.e. $\cos(\omega t)\cos(kx)$) does not. Often the first few modes account for most of the signal. We assess the relative contribution of each mode using

$$E_\ell = \frac{\lambda_\ell}{\sum_{j=1}^{M} \lambda_j} \,. \tag{3.7}$$

The implementation of the CEOF methodology is based on PCAtool (Maze, 2020).

3.3 Geomagnetic Secular Acceleration

We use the CHAOS-6-9x model to evaluate the geomagnetic acceleration at the core-mantle boundary (Finlay et al., 2016). The magnetic potential, V, is defined using time-dependent Gauss coefficients $\{g_n^m(t), h_n^m(t)\}$ in the form

$$V(r,\theta,\phi) = a \sum_{n=1}^{n_{max}} \sum_{m=0}^{n} [g_n^m(t)\cos m\phi + h_n^m(t)\sin m\phi] \left(\frac{a}{r}\right)^{n+1} P_n^m(\cos\theta)\,, \tag{3.8}$$

where the spherical coordinates (r,θ,ϕ) define radius, colatitude and longitude; P_n^m are the Schmidt quasi-normalized associated Legendre functions, and $a = 6371.2$ km is the average spherical radius of the surface. The radial component of the magnetic field is

$$B_r = -\frac{\partial V}{\partial r}\,, \tag{3.9}$$

so the geomagnetic acceleration is defined by

$$\ddot{B}_r = \frac{\partial^2 B_r}{\partial t^2} = (n+1) \sum_{n=1}^{n_{max}} \sum_{m=0}^{n} [\ddot{g}_n^m(t)\cos m\phi + \ddot{h}_n^m(t)\sin m\phi] \left(\frac{a}{r}\right)^{n+2} P_n^m(\cos\theta)\,, \tag{3.10}$$

where the time derivatives are evaluated using the spline representation in the CHAOS-6 model. We evaluate $\ddot{B}_r$ at the core-mantle boundary using $r = 3481$ km and $n_{max} = 13$. The time dependence of the CHAOS-6 model is sampled at 6-month intervals between 1998.5 and 2017.5. The spatial extent of our analysis is limited to three regions or windows, which we describe below as the Atlantic region, Southeast Asia and Alaska (see Fig. 3.1). Each of these windows exhibit active secular acceleration during the time interval of interest (Chulliat et al., 2010; Finlay et al., 2016). The bounding latitudes and longitudes for each window are listed in Table 3.1.

3.4 Description of the Leading-order CEOFs

The methodology from Section 3.2 is applied to $\ddot{B}_r$ on a geographic (θ,ϕ) grid within the selected window at six-month time intervals. Each CEOF describes a mode of variability in

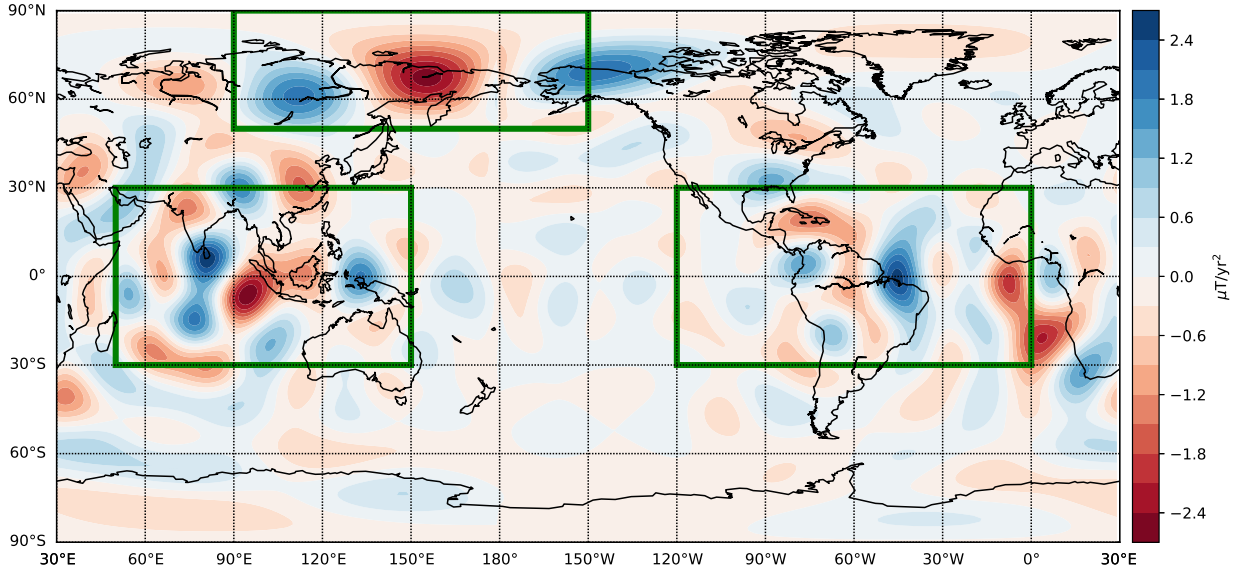

Figure 3.1: Secular acceleration of the geomagnetic field in 2011.0 from the CHAOS-6 model (Finlay et al., 2016). The three windows used in this study are displayed in green over the map.

Table 3.1: Bounding latitudes and longitudes for the geographic windows.

Window	East Longitude	West Longitude	North Latitude	South Latitude
Southeast Asia	50° E	150° E	30° N	30° S
Atlantic	120° W	0°	30° N	30° S
Alaska	90° E	150° W	90° N	50° N

θ, ϕ and t. We display these modes as functions of ϕ and t at fixed θ, but it is important to recognize that each CEOF gives a full description of the time variability in latitude and longitude. Our approach differs from previous applications of $\phi - t$ plots to detect waves (Chulliat et al., 2015; Finlay & Jackson, 2003) in that the individual CEOF modes have spatial coherence in latitude and longitude. Displaying the CEOF modes in $\phi - t$ plots at different latitudes reveals this coherence and allows us to quantify the uncertainty in the recovered wave properties (see below).

One example is illustrated in Fig. 3.2 for the geographic window below Southeast Asia. The left panel (a) shows a time-longitude plot of the original model for $\ddot{B}_r$ at a latitude of 7.2°. Spatial coherence in the CEOFs indicates that the choice of latitude within each window

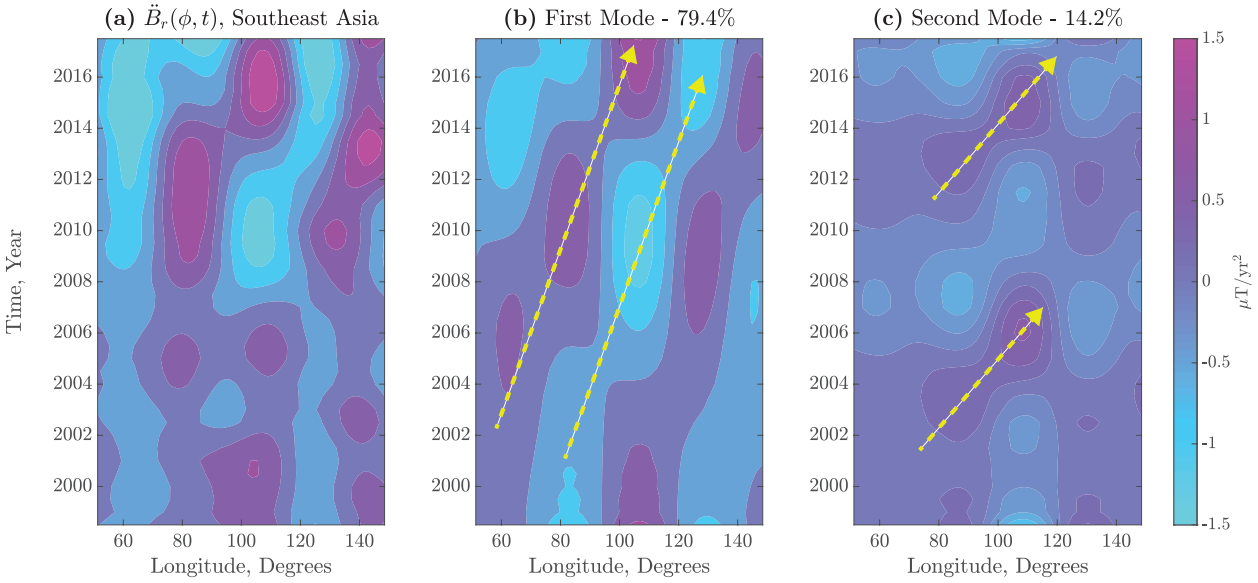

Figure 3.2: (a) Time-longitude plot of $\ddot{B}_r$ below Southeast Asia at latitude 7.2°. (b) Time-longitude plot of the first CEOF mode. An eastward propagating wave is identified with an angular order $m = 6$ and phase velocity $v = 3.81$ deg/yr (slope of yellow line). (c) Time-longitude plot of second mode reveals an eastward propagating wave with $m = 7$ and $v = 6.78$ deg/yr.

isn't critical, implying a similar pattern of time-longitude behavior across varying latitudes within a given window. Panels (b) and (c) of Fig. 3.2 show the corresponding results for the first and second CEOF. Evidence for eastward propagation of $\ddot{B}_r$ is seen in both (b) and (c) because positive and negative features in $\ddot{B}_r$ drift in the direction of positive longitude as time evolves. Superposition of the linear trends in (b) and (c) obscures the detection of trends in the original data.

The angular order, m, of the mode is inferred from the wavelength of variations in ϕ at fixed t and θ; the phase velocity, v, is recovered from the slope of the linear trend in $\ddot{B}_r$ as a function of ϕ and t. An estimate of the period, T, is computed from m and v, although it is also possible to make a direct estimate of T using the variations in $\ddot{B}_r$ at fixed ϕ and θ. A summary of results in Table 3.2 lists the average of properties recovered from three slope fits from twelve different values of θ across the window. Uncertainties are assigned to the averages on the basis on the standard deviation of the 36 samples. (While the angular order is assigned an integer value before computing the period, T, from the phase velocity v, we account for the standard deviation in both m and v when assigning an error to T). Modes that are not clearly identified as traveling waves are not assigned a wavenumber or a phase velocity.

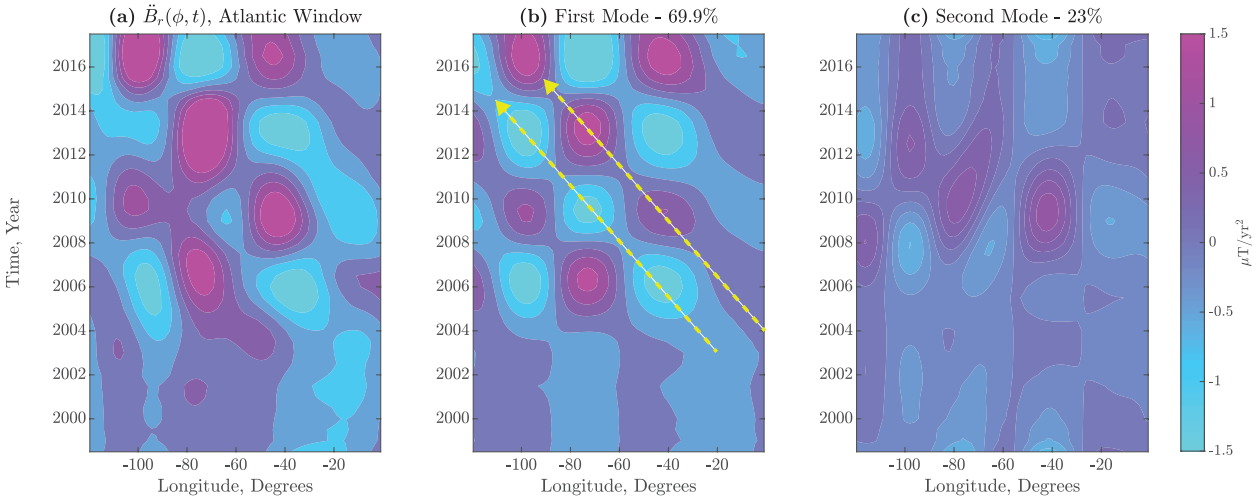

Figure 3.3: (a) Time-longitude plot of $\ddot{B}_r$ below the Atlantic window at latitude 2.7°. (b) Time-longitude plot for the first CEOF mode reveals a westward wave with angular order $m = 6$ and a phase velocity of $v = 8.48$ deg/yr. (c) Second CEOF mode does not represent a coherent traveling wave.

Table 3.2: A summary of wave properties for the three geographic regions. Unfilled entries indicate that the CEOF is not identified as a traveling wave.

Window	Mode	Weight (%)	Period (yr)	Wavenumber m	Velocity (deg/yr)	Velocity (km/yr)
Southeast Asia	1	79.4	15.73 ± 4.44	6	3.81 ± 0.93	232 ± 56
	2	14.2	8.73 ± 1.48	7	6.78 ± 1.08	411 ± 66
Atlantic	1	69.90	7.08 ± 0.58	6	-8.48 ± 0.58	-515 ± 35
	2	23.00	-	-	-	-
Alaska	1	94.7	20.75 ± 3.40	3	-5.78 ± 0.63	-132 ± 14
	2	4.40	-	-	-	-

Similar results are obtained for the other geographic windows. The first CEOF below the Atlantic region (Fig. 3.3) represents a westward traveling wave, whereas the second CEOF does not show clear evidence for a traveling wave. The first CEOF below Alaska also reveals a westward propagating waves (Fig. 3.4). Because this mode accounts for 94% of the signal there is not much difference between the first mode and the original data. By comparison the eastward traveling waves below Southeast Asia are less obvious in the original data (see

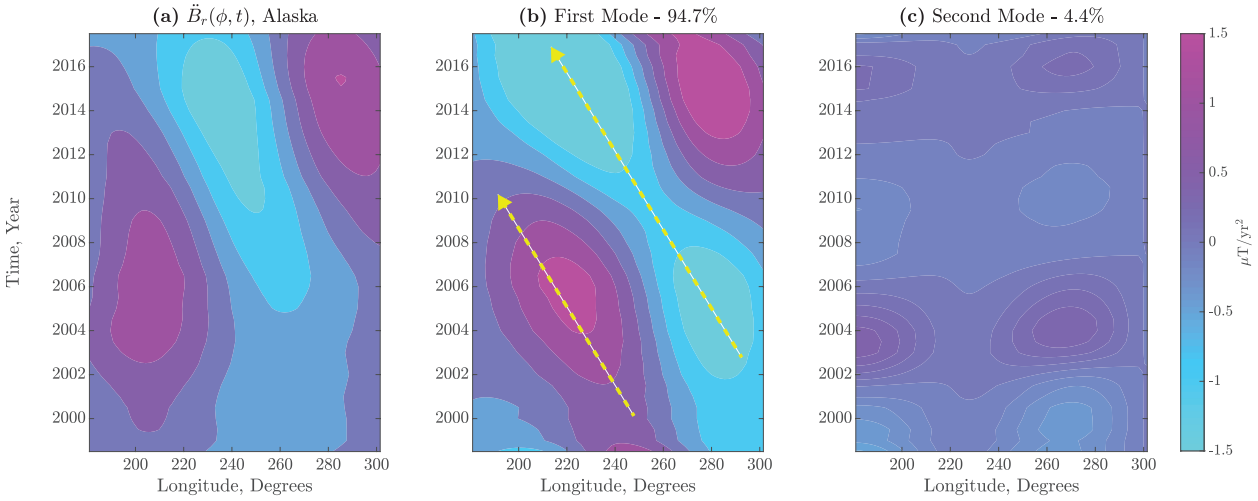

Figure 3.4: (a) Time-longitude plot of $\ddot{B}_r$ below the Alaskan window at latitude 65.7°. (b) Time-longitude plot of the first CEOF mode captures 94% of the variation; it is compatible with a westward wave at angular order $m = 3$ and phase velocity $v = 5.78$ deg/yr. (c) Second CEOF mode may represent a standing wave with a period of $T = 20.75$ yr.

Fig. 3.2)

The spatial coherence of the waves can be assessed by evaluating the correlation coefficient between individual $\phi - t$ plots at different values for θ. We select a reference value for θ near the center of the geographic window and compute the correlation coefficient as θ is shifted toward the limits of the window. The correlation coefficients for the equatorial regions is generally above e^{-1} when the waves are confined to roughly $\pm 20°$ (or less) in latitude. The first CEOF below Alaska is coherent between 55° and 85°.

Sources of uncertainty in the recovered CEOFs include the influences of measurement error and regularization in the CHAOS-6 model. Our results are also be affected by the duration of the record, especially when the mode period is comparable to the record length. To assess the influence of regularization we repeat the analysis using CHAOS-7 (Finlay et al., 2020). A much weaker regularization in CHAOS-7 puts more power in the secular acceleration. While both CHAOS models are highly correlated (about 78% for the SE Asia window), the corresponding CEOFs exhibit slightly higher correlation. This result is probably due to noise suppression by the CEOF methodology. Phase velocities for the first CEOF are consistent with the stated uncertainties. While some features of the field models may be due to the downward continuation of noise, our results are reproduced in models with different levels of smoothing.

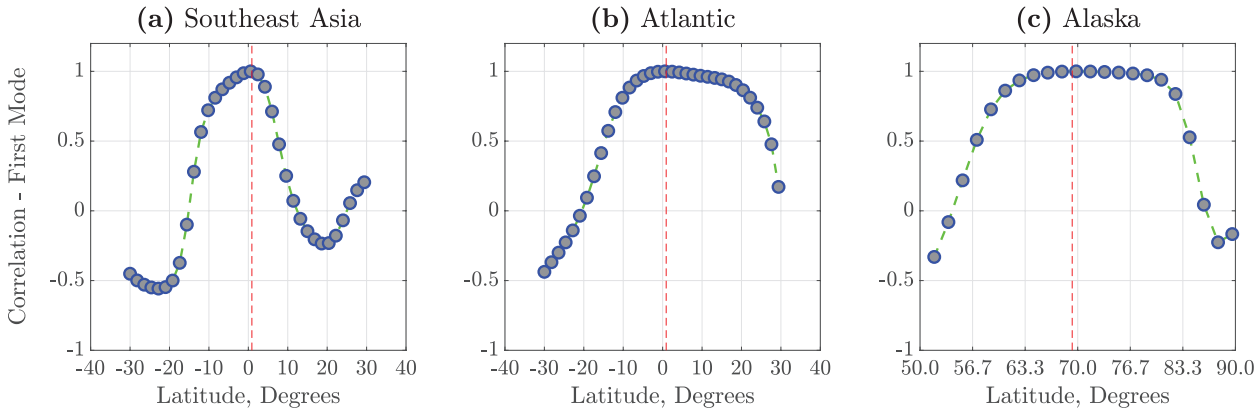

Figure 3.5: (a) Coherence of first CEOF in Southeast Asia is confined to latitudes $\pm 15°$ (b) Coherence of first CEOF in Atlantic window is confined to latitudes $\pm 20°$. (c) Coherence of first CEOF in Alaskan window is confined to latitudes $55° - 85°$.

The effect of record length is assessed by recovering the first CEOF from SE Asia using only 15 years of data. The phase velocity of the first mode is nearly unchanged but the period is shortened from 15.73 to 12.66 years. This change in period is accommodated by a small change in the angular order, but both these changes are within the reported uncertainties.

3.5 Interpretation of Waves

Application of the CEOF methodology to three geographic regions reveals evidence for both eastward and westward traveling waves. Similar conclusions were reached by Chulliat et al. (2015) using $\phi - t$ plots of secular acceleration in the equatorial region. Fourier transforms in both ϕ and t were used to identify the dominant angular orders and periods, yielding phase velocities of 550 ± 180 km/yr for waves with periods less than 10 years at $m = 6$. We obtain a similar range of phase velocities, 463 ± 74 km/yr, when the waves are restricted to periods less than 10 years.

The origin of the waves is constrained by the values recovered for the angular order, period and phase velocity. The fact that different wave properties are recovered in the different geographic regions suggests that several types of waves are generated by processes in the core. This heterogeneity supports our use of regional windows to analyze the secular acceleration.

Traveling waves can be represented in the general form, $f(\mathbf{x} - \mathbf{v}t)$, where $\mathbf{x}$ denotes the

position on the core-mantle boundary and $\mathbf{v}$ is the corresponding wave velocity. While $f(\mathbf{x} - \mathbf{v}t)$ obeys a wave equation, it also satisfies an advective equation

$$\frac{\partial f}{\partial t} + \mathbf{v} \cdot \nabla f = 0 \,, \tag{3.11}$$

which means that the recovered CEOFs cannot be used to distinguish between wave motion and advection. On the other hand, the velocities listed in Table 2 are probably too large to be due to fluid motion. Consequently, we favor a wave origin for the CEOFs.

Eastward traveling waves in the equatorial region of Southeast Asia are compatible with equatorially trapped MAC waves (Buffett & Matsui, 2019), denoted below as eMAC waves. Waves with angular order of $m = 6$ and periods of $T = 9$ to 16 years are compatible with eMAC waves in a stratified layer with a thickness of 25 to 30 km. Such a layer would require a buoyancy frequency, N, in excess of 5 times the rotation frequency (i.e. $N > 5\Omega$) to ensure that these waves are trapped in the equatorial region. Both the first and second modes in the Southeast Asia window can be reconciled with a single description of the stratification if the two modes have different equatorial symmetry (defined using the notation $n = 0$ and $n = 1$ in Buffett and Matsui (2019)).

A different type of wave is required below the Atlantic region because the dominant mode is westward propagating. This behavior is incompatible with the eastward propagating eMAC waves. An alternative candidate might be a type of localized Alfvén waves, as proposed by Aubert and Finlay (2019). These waves are detected in geodynamo simulations as disturbances that propagate from depth along tubes of magnetic field below the equatorial region of the core-mantle boundary. These authors note that the localized Alfvén waves appear to propagate to the west on arrival at the surface (Aubert & Finlay, 2019), so they may offer a viable explanation for the modes in the Atlantic region.

High-latitude waves below Alaska are also compatible with fluid stratification. A local beta-plane model (Braginsky, 1998a) predicts waves with a period of roughly 20 years in a stratified layer with a depth-averaged buoyancy frequency of $N = 0.52\Omega$ and a layer thickness of 140 km. The model assumes a constant buoyancy frequency, which we take to represent a depth-averaged N across the layer. Other combinations of thickness and stratification can also account for the predicted period, but we have chosen a thickness of 140 km to illustrate the compatibility with a previous study of zonal MAC waves (Buffett et al., 2016). That study adopted a depth-dependent buoyancy frequency with a maximum value of $N \approx \Omega$ at the core-mantle boundary, decreasing linearly to zero at the base of the layer. The corresponding depth-averaged buoyancy frequency is approximately 0.5Ω, in rough agreement with the value listed above. A more comprehensive numerical model for waves in a spherical shell (Knezek & Buffett, 2018) gives a roughly comparable period of $T = 22$ years for the same layer properties. The difference is probably due to the effects of spherical geometry at low wavenumber, although the details are not crucial because this difference is on the order

of the uncertainty in the recovered wave period (see Table 2). In addition, the numerical model predicts the nominal latitude of the wave motion. A mid-range latitude of 67° for the predicted wave is compatible with the window location below Alaska.

3.6 Conclusions

Complex EOFs are computed from the geomagnetic acceleration at the core-mantle boundary, allowing the observed time variation to be represented as a linear combination of traveling and standing waves. The first two CEOF modes typically account for more than 90% of the signal. We find evidence for eastward and westward traveling waves in the equatorial region, whereas westward traveling waves are detected at high latitudes. Both the high latitude and eastward traveling equatorial waves are compatible with fluid stratification at the top of the core.

Eastward traveling waves in the equatorial region require a thin layer (25-30 km) and strong stratification ($N > 5\Omega$), whereas the westward traveling waves at high latitudes require a thicker layer (≈ 140 km) and weaker stratification ($N \approx 0.5\Omega$). These results can be reconciled because a thick layer of thermal stratification is liable to produce a thin layer of strong stratification through barodiffusion of light elements (Gubbins & Davies, 2013). Equatorial waves are still expected in a thick stratified layer, but the predicted periods are several hundred years. Similarly, high-latitude waves are expected in a thin layer with strong stratification, but the periods could be less than one year. In both instances it may be difficult to detect these waves with the available observations.

Chapter 4

Signatures of High-Latitude Waves in Observations of Geomagnetic Acceleration

This work has been previously published as: Chi-Durán, R., Avery, M. S., & Buffett, B. A. (2021). *Signatures of high-latitude waves in observations of geomagnetic acceleration.* Geophysical Research Letters, 48, e2021GL094692. https://doi. org/10.1029/2021GL094692

Summary

Models for the second time-derivative of the geomagnetic field reveal prominent activity at high latitudes. Alternating patches of positive and negative geomagnetic acceleration propagate to the west at speeds that exceed nominal fluid velocities in the core. We show that waves are a viable interpretation of these observations. Magnetic Rossby waves produce a high-latitude response with suitable phase velocities. However, the spatial complexity of the prediction is not compatible with the observations. Our preferred interpretation involves zonal MAC waves. These waves can account for the observed geomagnetic field when a stratified layer exists at the top of the core. The required layer has a thickness in excess of 100 km and a buoyancy frequency comparable to the rotation frequency. We anticipate a gradual reduction in the phase velocity over time, leading to a future change in the propagation direction.

4.1 Introduction

Fluid motion in Earth's core produces variations in the geomagnetic field on a broad range of timescales (Korte et al., 2011; Olsen & Mandea, 2008). Short-period motion is most evident in the second time-derivative of the geomagnetic field (often called geomagnetic acceleration) because contributions from long-period motion are usually much weaker (Aubert & Gillet,

2021). This sensitivity enables the detection of short-period motion in satellite-based models of geomagnetic acceleration (Chulliat et al., 2010; Lesur et al., 2010). Several recent field models (Finlay et al., 2020; Ropp et al., 2020) reveal prominent activity at the core-mantle boundary below the equatorial region and at high-latitudes below Alaska. A common interpretation involves waves (Aubert & Finlay, 2019; Buffett & Matsui, 2019) because the observed features appear to propagate at speeds far in excess of the typical fluid velocity (Chi-Durán et al., 2020; Chulliat et al., 2015).

High-latitude activity below Alaska is characterized by a train of positive and negative patches that propagate westward at a velocity of 132 ($\pm$14) km yr^{-1}. This feature has an angular order $m = 3$, which yields a period of roughly 21 ($\pm$3) years (Chi-Durán et al., 2020). Possible interpretations include quasi-geostrophic Alfven waves (Aubert & Finlay, 2019) and magneto-Coriolis waves (Gerick et al., 2021). Both these waves are primarily confined to the equator, so we propose two other types of waves that are more compatible with the location and propagation characteristics of the observed features (see Fig. 4.1). One these of waves is sometimes called a magnetic Rossby wave (Braginsky, 1998b) because it propagates westward with a phase velocity that depends on the angular order of the fluid velocity. The second type of wave is a zonal MAC wave (Braginsky, 1993), which is characterized by a three-way force balance between magnetic, Archimedes (buoyancy) and Coriolis forces. Both of these waves depend on stable stratification at the top of the core. Radial motion through the stratified layer disturbs the radial profile of fluid density. Perturbations in hydrostatic pressure drive a nearly geostrophic flow. Because the fluid velocity for zonal MAC waves does not vary with longitude, the $m = 3$ structure of the geomagnetic acceleration is connected with the structure of the radial magnetic field. Much of this structure is associated with regions of stronger radial magnetic field at high latitudes. The phase velocity of the observed geomagnetic acceleration can be attributed to a projection effect as the fluid velocity and acceleration vary over a cycle (see Section 3.3).

In this study we show that both types of waves can account for the observed geomagnetic acceleration. Each interpretation requires a stratified layer and the properties inferred from the observations are broadly similar. However, we favor an interpretation based on zonal MAC waves, which requires a buoyancy frequency, N, comparable to the rotation frequency, Ω. This result is compatible with the properties recovered in a prior study (Buffett et al., 2016) of wave motion using the first time-derivative of the geomagnetic field.

4.2 Signature of Magnetic Rossby Waves

Magnetic Rossby waves are a natural explanation for the geomagnetic acceleration because the wave motion at low m is confined to high latitudes. A description of the waves using a beta-plane approximation (Braginsky, 1998b) predicts westward propagation with periods of 10–20 years when the top of the core is stratified. We replace the usual beta-plane ap-

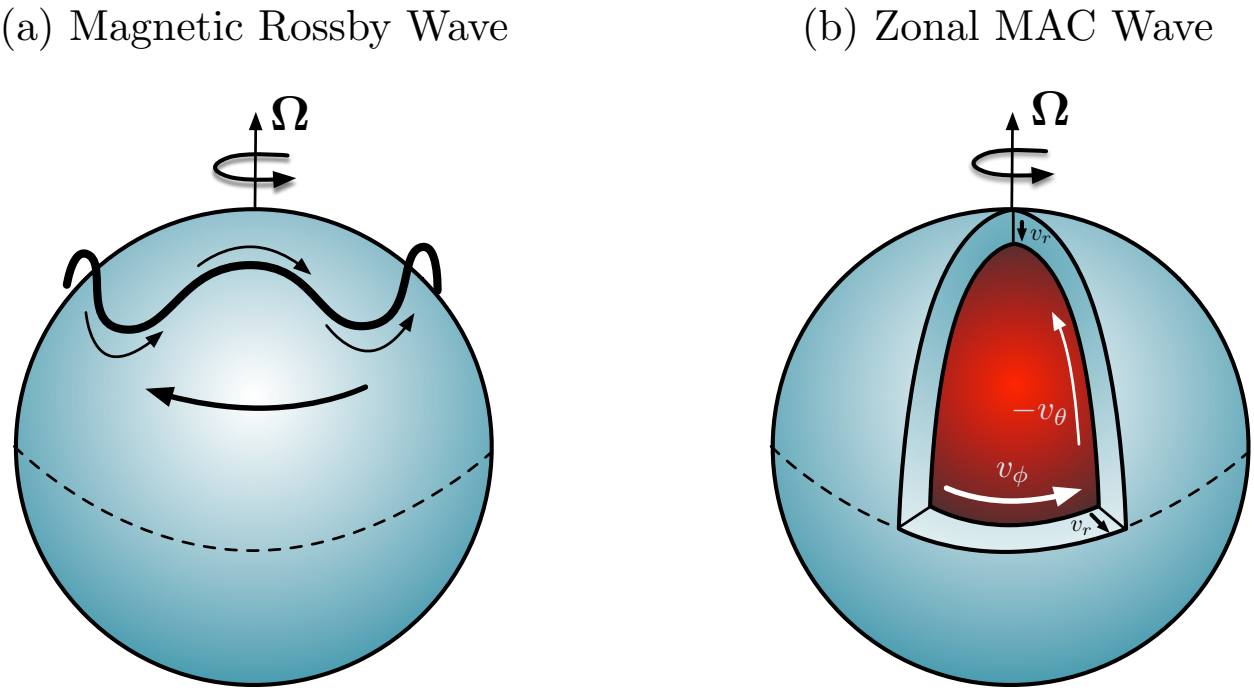

Figure 4.1: Schematic illustration of wave motions. (a) Magnetic Rossby wave with angular order $m = 3$. (b) MAC wave with $m = 0$ has azimuthal v_ϕ and meridional v_θ velocity at the core-mantle boundary. The weak v_θ component makes a small contribution to the geomagnetic acceleration.

proximation with a global description of waves in a spherical geometry. The results confirm that magnetic Rossby waves are restricted to high latitudes. In fact, these waves represent a westward traveling branch of the same dispersion relation that governs eastward traveling equatorial MAC waves in spherical geometries (see Appendix A).

Numerical solutions for the magnetic Rossby waves depend on the angular order of the wave motion, the radial magnetic field, as well as the strength, N, and thickness, H, of the stratified layer. Planetary-scale waves (e.g., $m = 3$) are less dependent on the toroidal magnetic field because the horizontal wavelength of flow is large compared with the radial lengthscale. A rough estimate for the relative importance of toroidal B_T and radial B_r magnetic fields in the dynamics is $mB_T H/(B_r\, R)$, where R is the radius of the core. Recent suggestions of strong toroidal fields in a stratified layer (Hardy et al., 2020) could make the toroidal field more important than expectations based on geodynamo models, although we do not consider this possibility here. Instead we adopt a constant rms radial field of 0.62 mT to be consistent with geodetic constraints (Koot et al., 2010). We note that wave motion is affected by the presence of radial magnetic field at all scales, including those too small to be

observed directly at the Earth's surface. However, once the wave motion is computed, we use the observed radial magnetic field to predict the observable contributions to geomagnetic acceleration.

The thickness and strength of the stratification are adjusted to match the position and phase velocity of geomagnetic acceleration from the CHAOS7 model (Finlay et al., 2020). A grid search over the model parameters shows that good agreement is possible with a limited (but finite) range of values for N and H . One solutions has $N = 0.6\Omega$ and $H = 132$ km, which yields a wave period of 21.1 years. A reasonable fit at the other end of the parameter range is obtained with $H = 84$ km and $N = 0.9\Omega$. We use the predicted fluid velocity and acceleration from the wave calculation to compute the expected geomagnetic acceleration. As a first approximation we assume a dipole for the radial main field, so the wave and geomagnetic acceleration have a common $m = 3$ structure. Additional structure is attributed to the equatorial component of the dipole. Both the position and phase velocity of the predicted geomagnetic acceleration are in good agreement with the CHAOS7 model (Finlay et al., 2020) (see Fig. 4.2b).

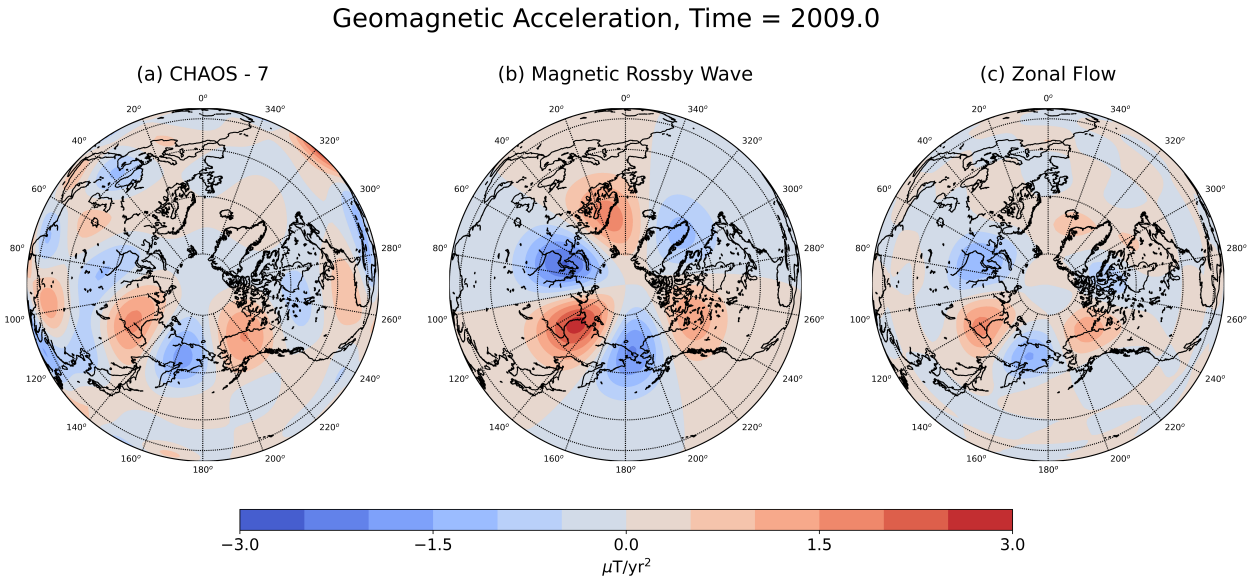

Figure 4.2: Comparison of wave models with observations. (a) Geomagnetic acceleration from CHAOS7 model (Finlay et al., 2020) at $t = 2009$. (b) $m = 3$ magnetic Rossby wave with $H = 132$ km and $N = 0.6\Omega$. (c) A purely zonal flow is used to represent zonal MAC waves. Patches of secular acceleration are evident in all three panels between longitudes 90° to 240°. Snapshots of the temporal evolution are included in the Appendix A.

Allowing for greater complexity in the main field introduces additional structure in the pre-

dicted geomagnetic acceleration. This complexity is evident in a time-longitude plot at a latitude of 66° N, which is close to the peak wave amplitude. (The peak amplitude is proximal to but unconnected with the location of the tangent cylinder.) When the main field is computed from CHAOS7 using a spherical harmonic expansion to degree $\ell = 12$ we predict longitudinal variations that include contributions with $m > 3$. Much of this additional structure is due to strong patches of radial magnetic field at high latitude. Because the predicted structure is not confined to $m = 3$ (see Fig. 4.3b), it appears that the fluid velocity and acceleration cannot be represented by a single wave at $m = 3$. This conclusion is independent of simplifications used in the wave model; any $m = 3$ wave will produce geomagnetic acceleration that is incompatible with the observations.

4.3 Signature of Zonal MAC Waves

One way to restrict the angular order of our prediction is to lower the value of m for the wave motion. Zonal MAC waves represent the end-member case because the flow is characterized by $m = 0$. This means that the structure of the resulting geomagnetic acceleration is entirely determined by the structure of the main field. Different waves within this class are specified by the principal spherical harmonic degree of radial motion through the stratified layer. The gravest mode at $\ell = 2$ corresponds to upward and downward radial motion at the pole and equator. The resulting pole-to-equator gradient in the hydrostatic pressure drives a perpendicular flow at mid-latitudes. Waves with higher ℓ have more rapid variations in latitude; these waves also have higher amplitudes near the poles.

To explore the viability of zonal MAC waves we recover estimates for the zonal flow and its acceleration using the CHAOS7 model. Accelerations in the zonal flow are then compared with predictions for zonal MAC waves to identify possible waves. We begin with the first time-derivative (secular variation), which is defined by

$$\dot{B}_r = -v_\phi \nabla_\phi B_r \tag{4.1}$$

where the azimuthal velocity, v_ϕ, is independent of longitude and $\nabla_\phi \equiv (R \sin\theta)^{-1} \partial_\phi$ denotes the azimuthal gradient (e.g., Buffett & Knezek, 2018; R. Holme, 2015). At each latitude and time we estimate a constant v_ϕ by minimizing the misfit to $\dot{B}_r$ using a bisection method. The procedure is repeated for the azimuthal acceleration, $\dot{v}_\phi$, using the definition of the second time derivative

$$\ddot{B}_r = -\dot{v}_\phi \nabla_\phi B_r - v_\phi \nabla_\phi \dot{B}_r \,. \tag{4.2}$$

We take B_r, $\dot{B}_r$ and $\ddot{B}_r$ from the CHAOS7 model and recover estimates for $\dot{v}_\phi$ using the previously computed value for v_ϕ. Our estimates for $\dot{v}_\phi$ account for slightly more than half the observed $\ddot{B}_r$ above a latitude of 50° N, based on the root-mean-square (rms) misfit, averaged over longitude and time. A similar calculation in the southern hemisphere reveals that zonal flow accounts for slightly less than 50% of $\ddot{B}_r$ poleward of 50° S (see Fig. A.1). The

overall amplitude of the observed and predicted geomagnetic acceleration in the Southern Hemisphere is weaker; the prediction is weaker due to smaller gradients in the large-scale B_r. In contrast to the polar regions, a zonal flow accounts for relatively little of the geomagnetic acceleration in the equatorial region, suggesting a different physical origin (Aubert & Finlay, 2019; Gerick et al., 2021).

Large-scale flow and magnetic field are not expected to contribute much more than 50% of the observed $\dot{B}_r$ and $\ddot{B}_r$ at short periods due to unmodeled effects in Eq. (1) and (2). Magnetic diffusion and small-scale flow can produce as much as half of the secular variations at periods less than 25 years (Gillet et al., 2019); a similar expectation extends to the geomagnetic acceleration. For this reason, it is striking to account for roughly 50% of $\ddot{B}_r$ with a very simple flow. The general spatial structure of the predicted geomagnetic acceleration agrees reasonably well with the observations away from the equator (see Fig. 4.2c and Fig. A.1). We also find good agreement in the overall time dependence, based on a representative time-longitude plot at 66° N (see Fig. 4.3c). Snapshots of the observations and predictions display the spatial and temporal dependencies together (see Appendix A).

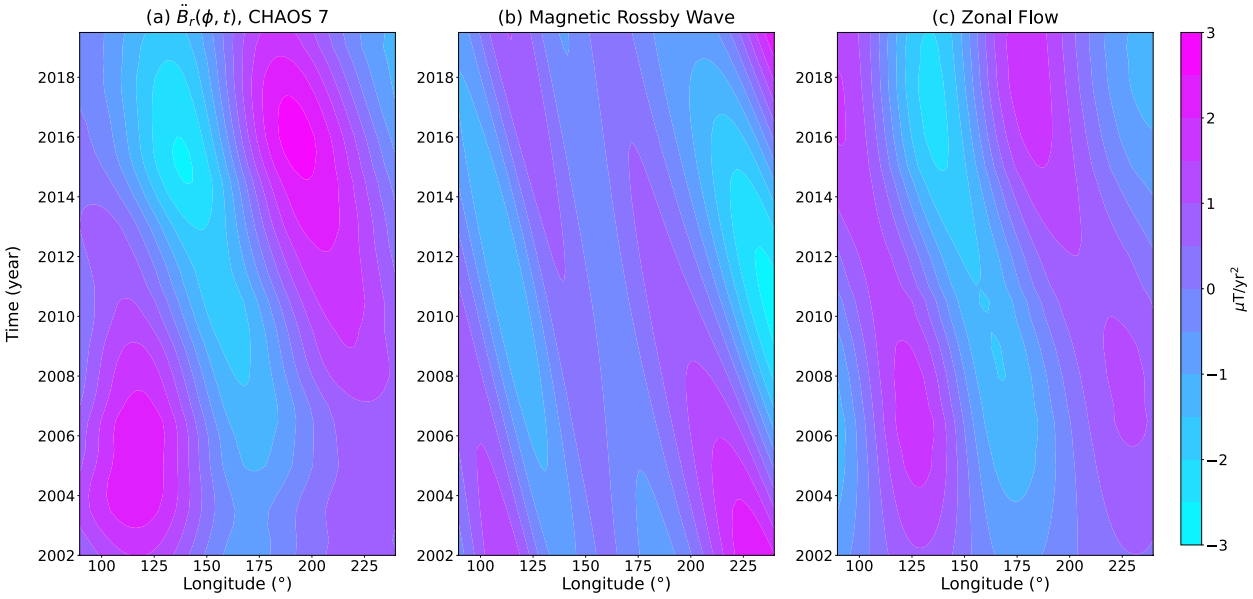

Figure 4.3: Time-longitude plot of $\ddot{B}_r$ in the active region. Longitudes are confined between 90° and 240° at latitude 66°N. (a) CHAOS7 model between 2002 and 2019.5. (b) Magnetic Rossby wave ($m = 3$) including the influence of radial magnetic field to degree $\ell = 12$. (c) A purely zonal flow is used to represent zonal MAC waves.

The velocity and acceleration used to construct the longitude-time plot are shown in Fig. 4.4. (Recall that constant values for v_ϕ and $\dot{v}_\phi$ are used at all longitudes for a specified

time.) The acceleration appears to oscillate with a roughly 20-year period about a slightly negative value; the nearly constant part of the acceleration could potentially represent a short segment of a longer period mode (Dumberry & Finlay, 2007; Livermore et al., 2017). The average acceleration over the 20-year interval is -0.6 km/yr, which is comparable in amplitude to the 0.4 km/yr acceleration predicted for 60-year MAC waves (Buffett et al., 2016). This means that the fluid accelerations recovered from CHAOS7 are compatible with the presence of long-period MAC waves. However, the relatively short satellite record makes it is difficult to isolate these waves.

4.4 Consequence for Fluid Stratification

A 20-year oscillation in the fluid acceleration (Fig. 4.4a) is compatible with predictions for zonal MAC waves. A more quantitative assessment depends on the characteristic degree ℓ of the wave structure. The fluid acceleration recovered from the CHAOS7 model is nearly symmetric about the equator (see Fig. 4.4c). We find that the spatial structure is broadly consistent with a $\ell = 8$ wave, although a single wave does not capture all aspects of the fluid acceleration. Modest improvements in the shape of the predicted wave are achieved when a constant rms radial field is replaced by one that increases from the equator to the pole by a factor of 1.85, consistent with the results of a recent high-resolution dynamo model (Buffett & Matsui, 2019). Apart from this one change there was no systematic attempt to tune the wave model to the fluid acceleration.

Because the period of zonal MAC waves is weakly dependent on the layer thickness, we take $H = 140$ km and let the buoyancy frequency increase linearly from the base of the stratified layer. The peak stratification N_{max} occurs at the core-mantle boundary, and the value required to reproduce a nominal period of 21 years is $N_{max} = 0.9\Omega$ for the fundamental mode (i.e., the simplest radial structure). Attributing the fluid acceleration to an $\ell = 6$ wave gives a slightly poorer match to the fluid acceleration but only changes the required stratification to $N_{max} = 1.4\Omega$. The quality factor for both the $\ell = 6$ and $\ell = 8$ waves is roughly $Q \approx 4$. (Here the quality factor is defined by $Q = 0.5\ \mathrm{Re}(\omega)/\mathrm{Im}(\omega)$, where ω is the wave frequency). Thinner layers lower the quality factor in proportion to H^2, so we favor a layer in excess of 100 km to avoid heavy damping. A more specific constraint on the wave damping is difficult because the record of fluid acceleration is relatively short.

It is evident from the longitude-time plot in Fig. 4.3c that a zonal flow can account for the phase velocity of the observed geomagnetic acceleration (Fig. 4.3a). Additional complexity in the high-latitude flow (Livermore et al., 2017) may represent a superposition of an $m = 1$ magnetic Rossby wave. However, our interpretation of the zonal flow is not altered by the presence of non-zonal waves. The rapid phase velocity of the observed geomagnetic acceleration is connected with the relative importance of fluid velocity and acceleration in Eq. (2). The leading-order term in $\ddot{B}_r$ is usually due to fluid acceleration. As the acceleration varies

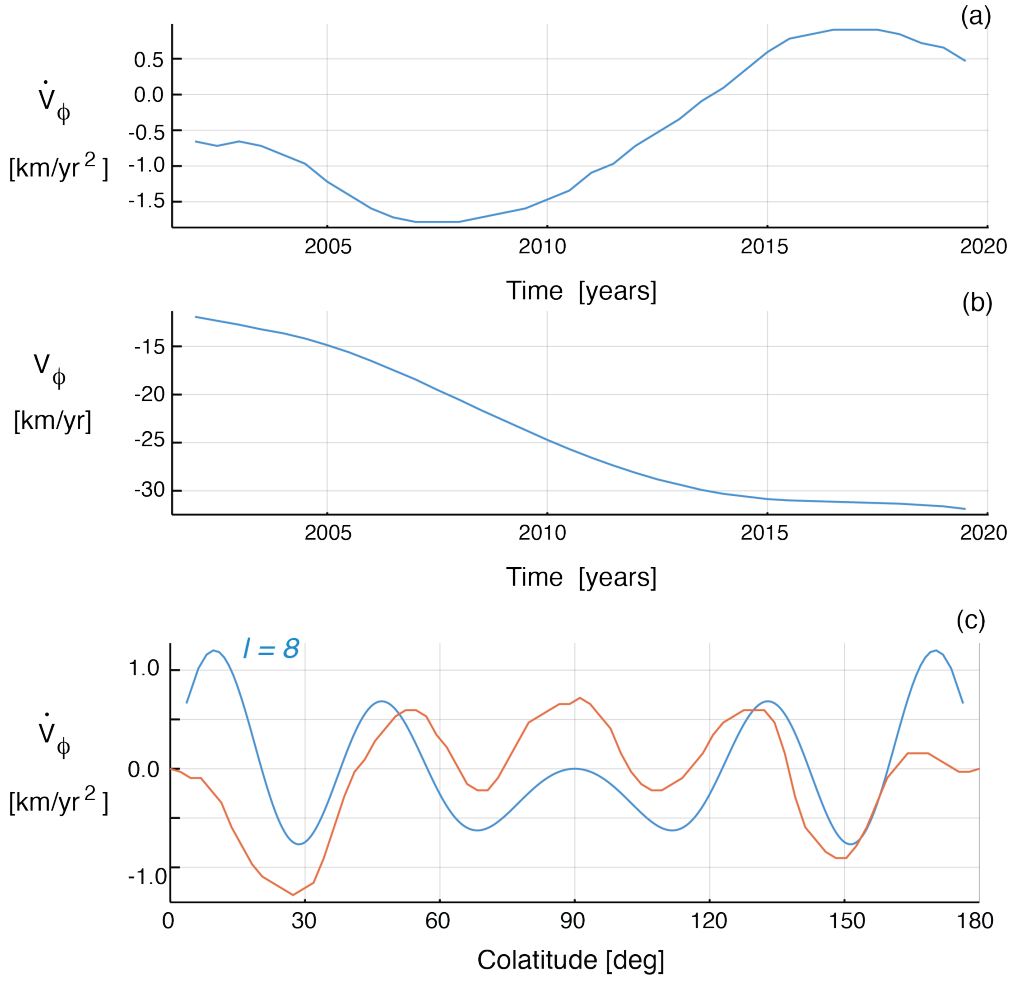

Figure 4.4: Zonal flow used to represent a MAC wave. (a) Acceleration and (b) velocity of flow recovered at latitude 66° N. Fluid acceleration fluctuates with a period of roughly 20 years about a negative average value. (c) Spatial structure of fluid acceleration in 2006 (red) compared with a zonal MAC wave (black). Reasonable agreement in the colatitude of maxima and minima is achieved with an $\ell = 8$ wave. Discrepancies are evident in the immediate vicinity of the poles.

over a cycle we expect its contribution to $\ddot{B}_r$ to fluctuate without causing any propagation in longitude. However, the fluid acceleration term must vanish over the cycle of a wave. In this case the second term involving v_ϕ and $\dot{B}_r$ becomes the main contribution to $\ddot{B}_r$. It is precisely during this transition that we observe the rapid phase velocity. Outside of this transition interval the phase velocity is expected to be small. Indeed there is evidence prior to 2004 that the phase velocity of the geomagnetic acceleration is small (see Fig. 4.3a), consistent with our expectations for zonal MAC waves. Further, based on this MAC wave

interpretation, we anticipate a gradual reduction in the phase velocity in the next ∼5 years (Fournier et al., 2021), followed by a change in the propagation direction.

4.5 Conclusions

Two types of waves can account for geomagnetic acceleration at high latitudes. Magnetic Rossby and zonal MAC waves can reproduce the angular order and frequency of the geomagnetic acceleration. However, the spatial structure of the radial geomagnetic field adds complexity to the predictions of magnetic Rossby waves, which is not evident in the observations. By comparison the predictions of zonal MAC waves are more consistent with the observed spatial pattern of $\ddot{B}_r$. Both wave models require a stratified layer at the top core. Values for the thickness and strength of stratification are broadly consistent for the two wave models and with previous estimates. The buoyancy frequencies are comparable to the rotation rate, which is a property commonly attributed to thermal stratification. Our predictions should be testable in the next few years. We expect a gradual reduction in the phase velocity, followed by a reversal in the propagation direction.

Chapter 5

Extracting spatial–temporal coherent patterns in geomagnetic secular variation using dynamic mode decomposition

This work has been previously published as: Chi-Durán, R., & Buffett, B. A. (2023). *Extracting spatial–temporal coherent patterns in geomagnetic secular variation using dynamic mode decomposition*. Geophysical Research Letters, 50, e2022GL101288. https://doi.org/10.1029/2022GL101288

Summary

Rapid growth of magnetic-field observations through SWARM and other satellite missions motivate new approaches to analyze it. Dynamic mode decomposition (DMD) is a method to recover spatially coherent motion with a periodic time dependence. We use this method to simultaneously analyze the geomagnetic radial field and its secular variation from CHAOS-7 at high latitudes. A total of five modes are permitted by noise levels in the observations. One mode represents a slowly evolving background state, whereas the other four modes describe a pair of waves; each wave is comprised of a complex DMD mode and its complex conjugate. The waves have periods of $T_1 = 19.1$ and $T_2 = 58.4$ years and quality factors of $Q_1 = 11.0$ and $Q_2 = 4.6$, respectively. A 60-year wave is consistent with previous predictions for zonal waves in a stratified fluid. The 20-yr wave is also consistent with previous reports at high latitudes, although its nature is less clear.

5.1 Introduction

Observations of the geomagnetic field offer a wealth of information about the dynamics of Earth's deep interior. Historical records from the past 400 years (Jackson et al., 2000) are commonly used to construct models of the geomagnetic field and its first time derivative, often called secular variation. A large part of the secular variation is attributed to large-scale fluid motion near the surface of Earth's core (e.g. Holme et al. (2015)). Other contributions include magnetic diffusion and the effects of unresolved small-scale flow. Recent efforts to account for these effects (Gillet et al., 2019) rely on geodynamo simulations to establish statistical correlations between the predicted flow and the magnetic field. While this approach represents the forefront of current research, it does mean that our ability to recover dynamics from magnetic-field observations is dependent on prior assumptions about the nature of flow. A complementary approach relies on modern data-driven methods to identify and characterize patterns of change in the observations. One particular technique, known as *dynamic mode decomposition* (Schmid, 2022), is particularly well-suited to the analysis of magnetic-field observations because it allow us to establish modes (waves) in the data before attaching a physical interpretation. There is no requirement for each mode to have a common physical basis or interpretation, although we do expect a common set of background conditions. A primary motivation for this study is to explore the feasibility of using new data-driven approaches to assess the geomagnetic field.

Several factors prompt our interest in data-driven approaches. One is the availability of magnetic observations from satellite missions (e.g. *Orsted, CHAMP, SWARM*), which substantially improve the quality and quantity of information. Satellite-based observations give better spatial coverage and allow greater discrimination between the internal and external sources of the geomagnetic field compared to ground-based measurements (Friis-Christensen et al., 2006). This improvement in observations has occurred in parallel with advances in the methods used to construct geomagnetic field models. Weaker temporal regularization and more flexible descriptions of the time dependence (Barrois et al., 2018; Finlay et al., 2016; Gillet et al., 2013; Olsen et al., 2006) have enabled reliable estimates of the second time derivative of the geomagnetic field (known as secular acceleration). This information creates new opportunities for exploring the dynamics of Earth's core on timescales that are surprisingly short. Short pulses of secular acceleration have been detected in the equatorial region (Chulliat et al., 2010; Finlay et al., 2016) and at high latitudes below Alaska (Chi-Durán et al., 2020; Finlay et al., 2020). The duration of these events is sometimes only a few years, and the equatorial disturbances often coincide with magnetic jerks (Chulliat & Maus, 2014).

Observations of secular acceleration point to much richer dynamics on short timescales (Finlay et al., 2020). The origin of these fluctuations is not well understood, although several lines of evidence from geodynamo models point to hydromagnetic waves in the core (Aubert & Gillet, 2021). Additional evidence comes from models of secular acceleration (Chi-Durán

et al., 2020). A snapshot of secular acceleration from the CHAOS-7 model (Finlay et al., 2016) in 2008.5 shows regions of high activity near the equator and at high latitudes (see Fig. B.1 in Appendix B). Disturbances propagate at velocities of several hundred km/yr, which is more than an order of magnitude faster than the largest fluid velocities inferred from secular variation. Waves are a viable interpretation of these rapid disturbances, and the DMD methodology is an ideal detection tool because it identifies spatially coherent structures with a periodic time dependence (see Section 5.2).

5.2 Dynamic Mode Decomposition

Dynamic mode decomposition (DMD) is a method to recover the dynamics of a physical system from observations (Schmid, 2010). It was originally devised for linear systems in the context of fluid mechanics (Schmid, 2011), although recent theoretical developments have paved the way for extensions to nonlinear systems (Rowley et al., 2009). To illustrate the fundamental concept we consider a linear system

$$\frac{d\mathbf{f}}{dt} = \mathbf{A}\mathbf{f} \tag{5.1}$$

for the time dependence of a vector $\mathbf{f}(t)$. Here $\mathbf{A}$ is a constant matrix and the elements of $\mathbf{f}$ might represent the values of a function on a spatial grid x_i $(i = 1, \ldots, n)$. A general solution for an arbitrary time increment Δt is

$$\mathbf{f}(t_0 + \Delta t) = e^{\mathbf{A}\Delta t}\mathbf{f}(t_0) \equiv \tilde{\mathbf{A}}\,\mathbf{f}(t_0) \tag{5.2}$$

where $\mathbf{f}(t_0)$ denotes the initial condition at $t = t_0$. The goal of the DMD method is to recover an estimate for the finite-time matrix $\tilde{\mathbf{A}}$ using pairs of snapshots of the system. We define a data matrix

$$\mathbf{F} = [\mathbf{f}(t_0)\ \mathbf{f}(t_1)\ ..., \mathbf{f}(t_{m-1})] \tag{5.3}$$

and let

$$\mathbf{F}' = [\mathbf{f}(t_1)\ \mathbf{f}(t_2)\ ..., \mathbf{f}(t_m)] \tag{5.4}$$

be the data matrix at a subsequent snapshot (e.g.. $t_k = t_{k-1} + \Delta t$). An optimal approximation for $\tilde{\mathbf{A}}$ minimizes the misfit to

$$\mathbf{F}' = \tilde{\mathbf{A}}\mathbf{F}\,. \tag{5.5}$$

Once we establish the matrix operator $\tilde{\mathbf{A}}$ from Eq. 5, we can evolve the system forward in time using

$$\mathbf{f}(t_k) = \tilde{\mathbf{A}}\mathbf{f}(t_{k-1})\,. \tag{5.6}$$

Several implementations of the DMD method have been proposed (e.g. Brunton and Kutz (2019) and Schmid (2022)). We follow the approach called exact DMD (Tu et al., 2014), which differs slightly in the way the eigenvectors of $\tilde{A}$ are computed. The eigenvalues and eigenvectors of $\tilde{\mathbf{A}}$ define the dynamic modes, although in practice the modes are computed

by first projecting $\tilde{\mathbf{A}}$ onto the leading principal components (singular vectors) of the data matrix $\mathbf{F}$. In effect, we use coherent spatial structure from the data matrix to construct $\tilde{\mathbf{A}}$ (see Tu et al. (2014) for details). When r singular values are retained in the singular value decomposition of $\mathbf{F}$, the reconstruction of the data can be written as

$$\mathbf{f}(t_k) = \sum_{j=1}^{r} \mathbf{\Phi}_j [\tilde{\lambda}_j]^k b_j \tag{5.7}$$

where $\mathbf{\Phi}_j$ is the eigenvector and $\tilde{\lambda}_j$ is the eigenvalue of $\tilde{\mathbf{A}}$, which has been raised to the kth power in Eq. 7; b_j defines the mode amplitude, such that the initial condition can be written as a linear combination of the modes

$$\mathbf{f}(t_0) = \sum_{j=1}^{r} \mathbf{\Phi}_j b_j \,. \tag{5.8}$$

We can express Eq. 5.7 in a more convenient form by noting that the eigenvalues of $\tilde{\mathbf{A}}$ are related to the eigenvalues λ_j of the original $\mathbf{A}$ matrix in Eq. 1 (e.g., Perko (2013)). Letting

$$\tilde{\lambda}_j = \exp(\lambda_j \Delta t) \tag{5.9}$$

allows us to rewrite the data reconstruction as

$$\mathbf{f}(t_k) = \sum_{j=1}^{r} \mathbf{\Phi}_j [e^{\lambda_j k \Delta t}] b_j \tag{5.10}$$

where we see that the time dependence of the system is explicitly recovered through the DMD procedure. We can think of the DMD modes as a linear combination of principal components (or EOFs) that evolve with a complex frequency λ. This makes DMD ideal for detecting waves in magnetic-field models because any coherent wave structure is expected to have a specific frequency. In general the frequencies will be complex (i.e. $\lambda = \sigma_j + i\omega$) so we can define the quality factor (Q) of a mode as

$$Q_j = \frac{\omega_j}{2\sigma_j} \,. \tag{5.11}$$

This quantity, Q, is used to quantify the damping of the waves. Finally, it is important to note that complex eigenvalues appear as complex conjugate pairs when the input data is real; if λ is a complex eigenvalue of $\mathbf{A}$ then the complex conjugate λ^* is also an eigenvalue of $\mathbf{A}$. This means that a pair of DMD modes have the same frequency ω.

5.3 Results

We model the geomagnetic radial field and secular variation simultaneously by defining a state vector as (see Eq. 5.1)

$$\mathbf{f} = \begin{bmatrix} \mathbf{B_r} \\ \dot{\mathbf{B}}_\mathbf{r} \end{bmatrix} \tag{5.12}$$

where $\mathbf{B_r}$ and $\dot{\mathbf{B}}_\mathbf{r}$ are the geomagnetic radial field (in 10^{-9} [T]) and secular variation (in 10^{-10} [T/yr]), respectively from CHAOS-7.12 (Finlay et al., 2020). (The choice of units is intended to give slightly higher weight to the time rate of change of secular variation in the construction of the system matrix A.) The augmented state vector means that our linear system in Eq. 5.1 corresponds to the coupled equations for secular variation and secular acceleration. The state vector is evaluated between 1998 and 2019 using a geographic grid with 100 grid points in latitude and 200 grid points in longitude. We restrict the DMD analysis to the Northern Hemisphere between latitudes 30°N and 90°N. The number of modes used in the calculation is set by the level of coherence in the observations (see next Section). We use 5 singular values in the construction of the DMD modes to produce 5 modes. The first mode describes a secular trend with an infinite period (zero frequency). We interpret this mode as the slowly evolving structure of the main field and secular variation. The other four modes represent two waves with periods of 19.1 and 58.4 years and quality factors of 11.0 and 4.6, respectively. The spatial structure of the four wave-like modes is shown in Fig. 5.1. The corresponding time dependence of each modes is shown in Fig. 5.2. These specific predictions are obtained when the CHAOS-7 model is truncated at degree $\ell = 14$. Small changes in the periods are found when the truncation is increased, whereas the spatial structures of the modes are nearly invariant.

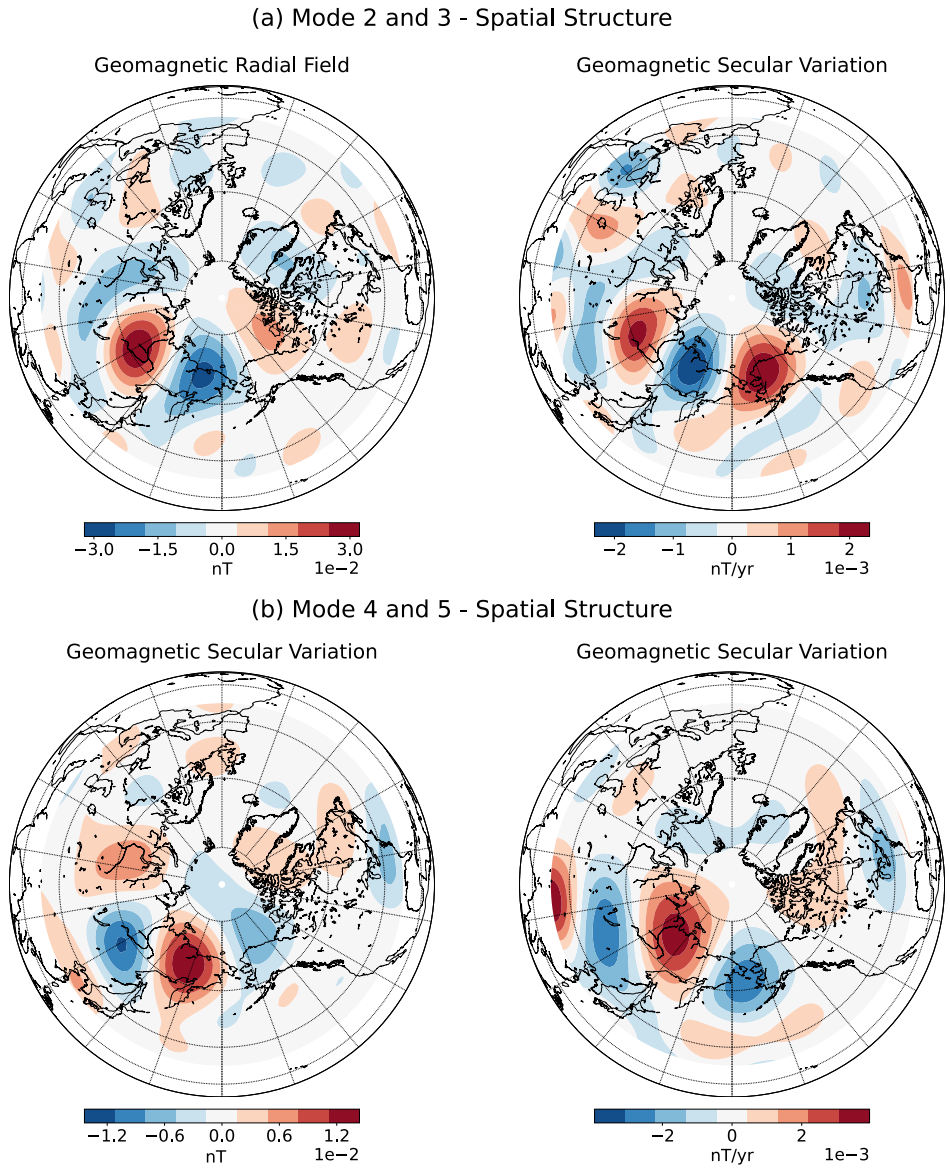

Figure 5.1: (a) Spatial structure of the Modes 2 and 3 with a period of 58.4 years. (b) Spatial structure of the Modes 4 and 5 with a period of 19.2 years. To reconstruct the magnetic field and secular variation at a given time, it is necessary to multiply the modes by their amplitudes b_i and by their temporal dependence (see Figure 5.2).

A superposition of the first 5 DMD modes accurately reconstructs the original signal from CHAOS-7 (Fig. 5.3a). For example, Mode 1 in Fig. 5.3b gives a reasonable description of the main field. Adding Modes 2 and 3 to Mode 1 captures most of the variability in CHAOS-7 (compare Fig. 5.3a and Fig. 5.3c). Adding Modes 4 and 5 (see Fig. 5.3d) produces only

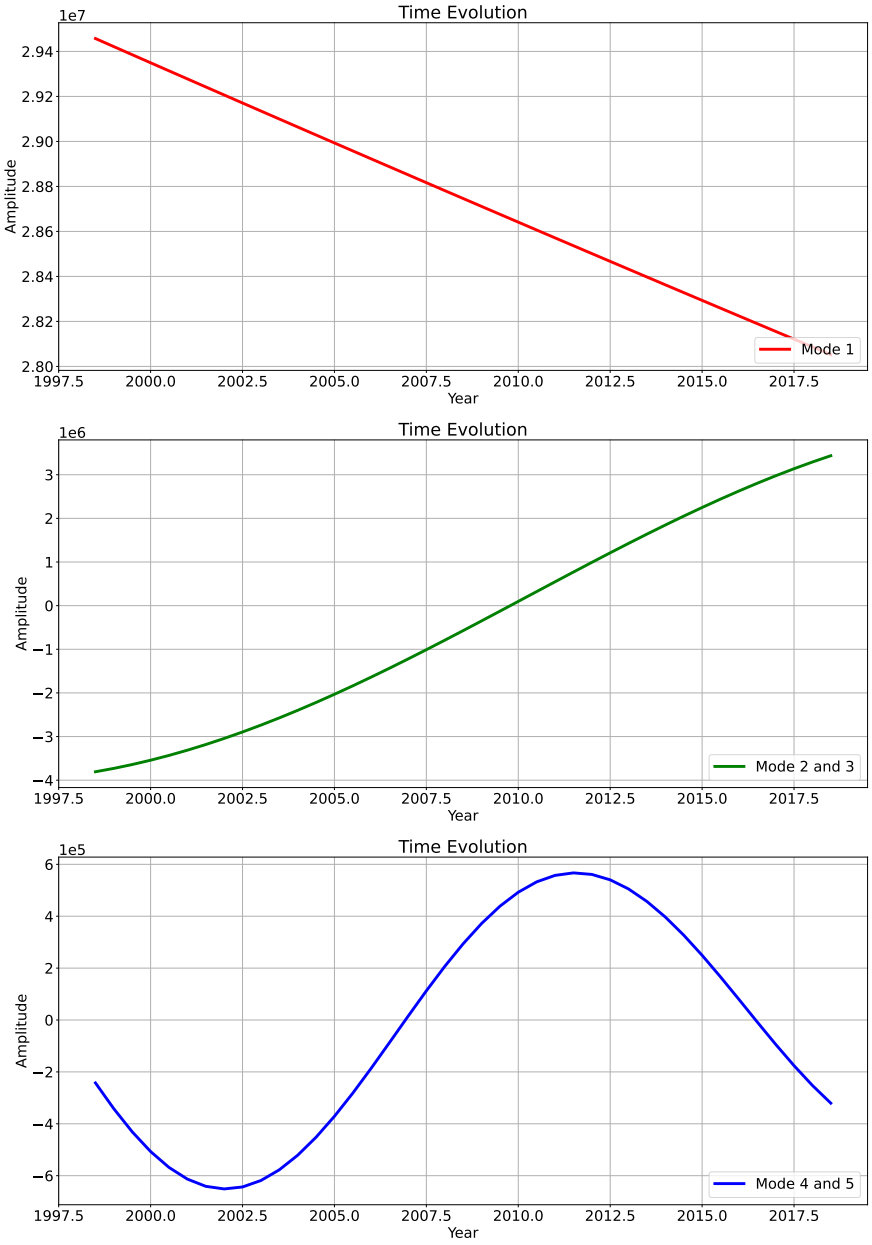

Figure 5.2: (a) Temporal evolution of Mode 1. This mode represents a secular trend with an infinite period. (b) Temporal evolution of Modes 2 and 3 corresponds to a period of 58.4 years and quality factor of 4.6. (c) Temporal evolution of Modes 4 and 5 corresponds a period of 19.1 years and quality factor of 11.0.

small changes in the reconstruction. We conclude that the first five modes are sufficient to recover most of the original signal.

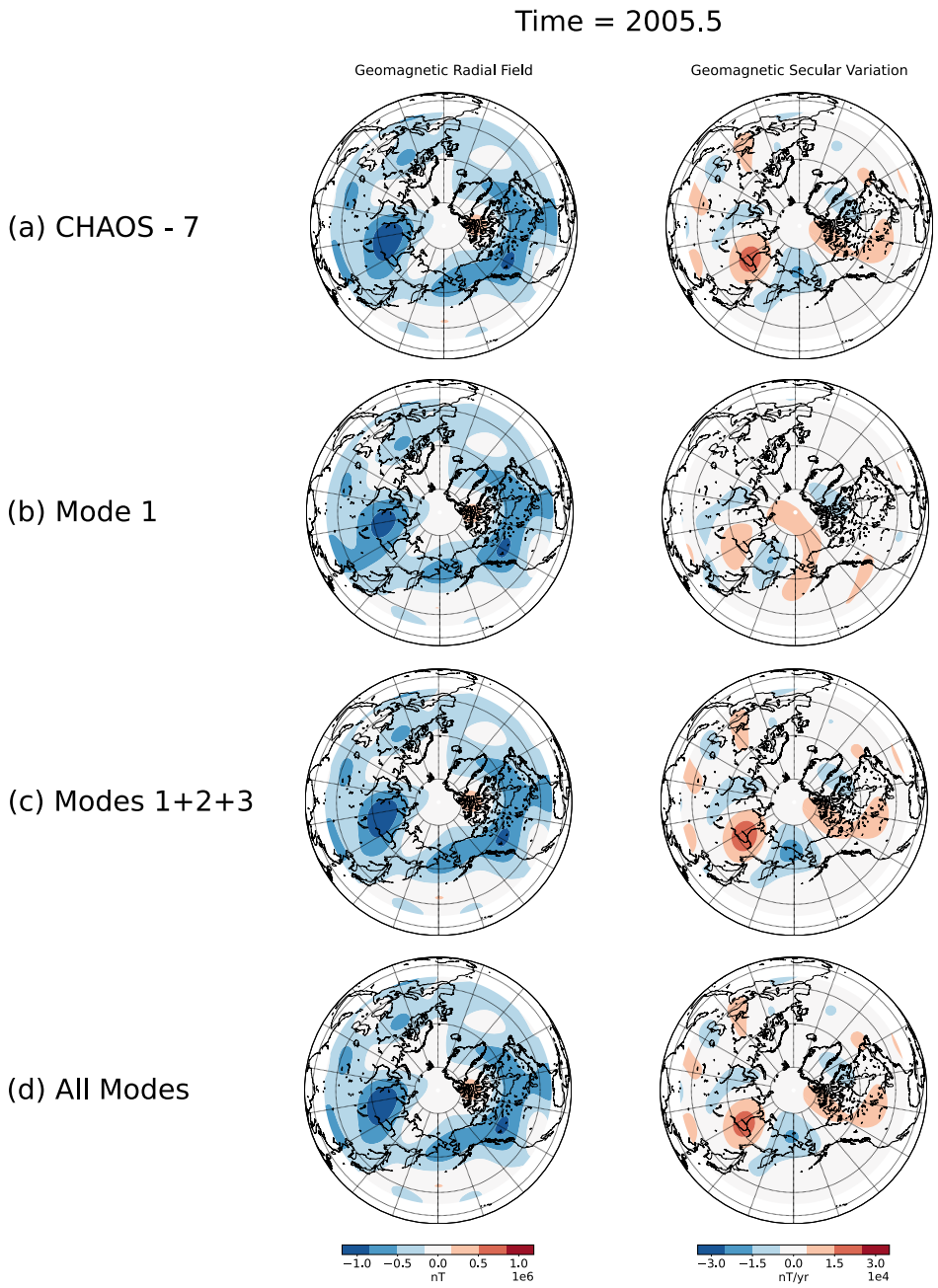

Figure 5.3: (a) Geomagnetic radial field and geomagnetic secular variation from CHAOS7. (b) Geomagnetic radial field and geomagnetic secular variation from Mode 1 (c) Geomagnetic radial field and geomagnetic secular variation using the superposition of modes 1, 2 and 3 (c) Geomagnetic radial field and geomagnetic secular variation using all modes (1, 2, 3, 4 and 5). All quantities are calculated at $t = 2005.5$ using $\ell = 14$ for the model truncation.

5.4 Discussion

Application of the DMD methodology to the Northern Hemisphere reveals three distinct types of variability in the geomagnetic field. We detect a slow secular trend and two damped waves. The fact that distinct wave features are recovered by the DMD method means that we are finding coherent spatial and temporal structure in the CHAOS-7 model. We now turn to the question of whether we can identify the origin of this coherent structure.

Mode 1 represents a steady trend in the geomagnetic field. The amplitude of the recovered mode increases linearly at a rate of about 0.3% per year (see Figure 5.2a). The eigenvalue of Mode 1 is purely real, which means that ω vanishes and the period $2\pi/\omega$ is infinite. This mode accounts for the spatial structure of the geomagnetic radial field and its slow secular trend. Deviations from this secular trend are described by the other DMD modes.

The oscillatory modes are needed to reconstruct short-period variations in the original signal. The most prominent feature in B_r and $\dot{B}_r$ is due to a mode with a nominal 60-year period. Figure 5.4 shows the average misfit between the reconstruction and CHAOS-7 using a different combination of modes. The average misfit is calculated as the average of absolute value of the difference between the reconstruction of the signal (superposition of modes) and the original data. The total misfit is divided by the number of grid points in the sum. Reconstructions that do not include the 60-year variation in Modes 2 and 3 have a higher misfit in both the radial magnetic field and the secular variation. By comparison, Modes 4 and 5 contribute much less to the variation. This can be seen by comparing the misfit for Modes 1, 2 and 3 with that for Modes 1, 4 and 5 (see Fig. 5.4). The first combination (Modes 1,2, and 3) lowers the average misfit by approximately one of magnitude relative to the second combination (Modes 1, 4, and 5). On the other hand, there is a discernible improvement in the misfit to B_r and $\dot{B}_r$ when all five modes are included. The time average misfit using all five modes corresponds 0.1% in the geomagnetic radial field and 11% in the geomagnetic secular variation.

A nominal 60-year wave in the secular variation is broadly consistent with previous studies (Roberts et al., 2007; Yokoyama & Yukutake, 1991). One possible interpretation of the 60-year variation is due to a zonal MAC wave, which depends on the existence of stable stratification at the top of the core. Buffett et al. (2016) showed that a zonal MAC wave, identified by spherical harmonic degree $\ell = 4$, could account for fluctuations in both the geomagnetic field and the length of day. In this study we reproduce the predictions for an $\ell = 4$ MAC wave using a physical model that allows for latitudinal changes in the rms radial magnetic field (Buffett & Knezek, 2018). Here we let the mean-square radial field increase by a factor of 3.5 between the equator and the pole, consistent with predictions from dynamo models. The overall intensity of the radial field is defined to have a surface-averaged rms strength of 0.5 mT. Predictions with this choice of rms radial field provide a reasonable fit to the spatial structure of Modes 2 and 3 (only Mode 3 is shown in Figure 5.5. The

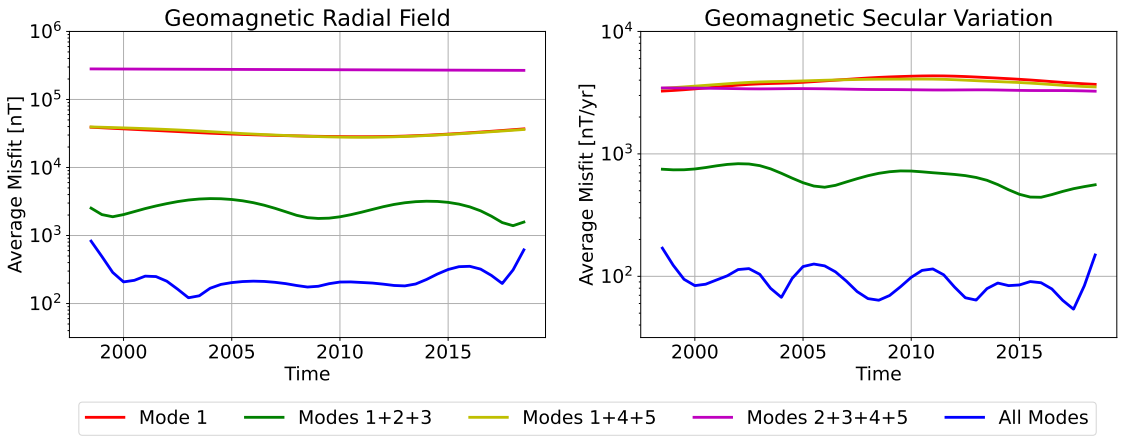

Figure 5.4: Misfit to the geomagnetic radial field and the geomagnetic secular variation over time when different modes are included in the reconstruction.

most prominent features in Mode 3 are the alternating patches of secular variation below Siberia and Alaska. A similar pattern of secular variation is also evident in the predictions for the $\ell = 4$ MAC wave, although there are notable differences. In particular, we find a strong negative patch in the secular variation below central Asia, which is much weaker in the DMD mode. There also appears to be a 20° shift in the longitude of the peak variations at high latitudes. Further differences below the Atlantic and Greenland also contribute to a surprisingly large $\mathcal{O}(1)$ misfit, despite the qualitative visual similarity of the two signals. Other MAC waves with higher ℓ have greater spatial complexity, which introduces features that are not seen in Mode 3.

Estimates for the period and damping of Mode 3 constrain the choice of physical properties for the wave model. Of particular interest is the thickness and strength of stable stratification at the top of the core. To be specific we allow a linear variation in buoyancy frequency N across the layer, starting with a value $N = 0$ at the base of the layer. In this case the layer properties are fully defined by the layer thickness and the peak buoyancy frequency at the core-mantle boundary. To illustrate we consider a 140-km thick layer with a peak buoyancy frequency of $N_{max} = 0.86\Omega$, where Ω is the Earth's rotation frequency. An $\ell = 4$ MAC wave has a period of 58.4 years and a quality factor $Q = 2.8$, which is broadly compatible with the complex frequency of Modes 2 and 3. Weaker secular variation due to waves in the southern hemisphere is expected because the horizontal gradients in the radial field are smaller in this region.

The DMD method also identifies a nominal 20-year wave, which has been previously reported in the Northern Hemisphere (Chi-Durán et al., 2021; Chi-Durán et al., 2020). However, the origin of Modes 4 and 5 is less clear. It is reasonable to ask if the 20-year wave could be

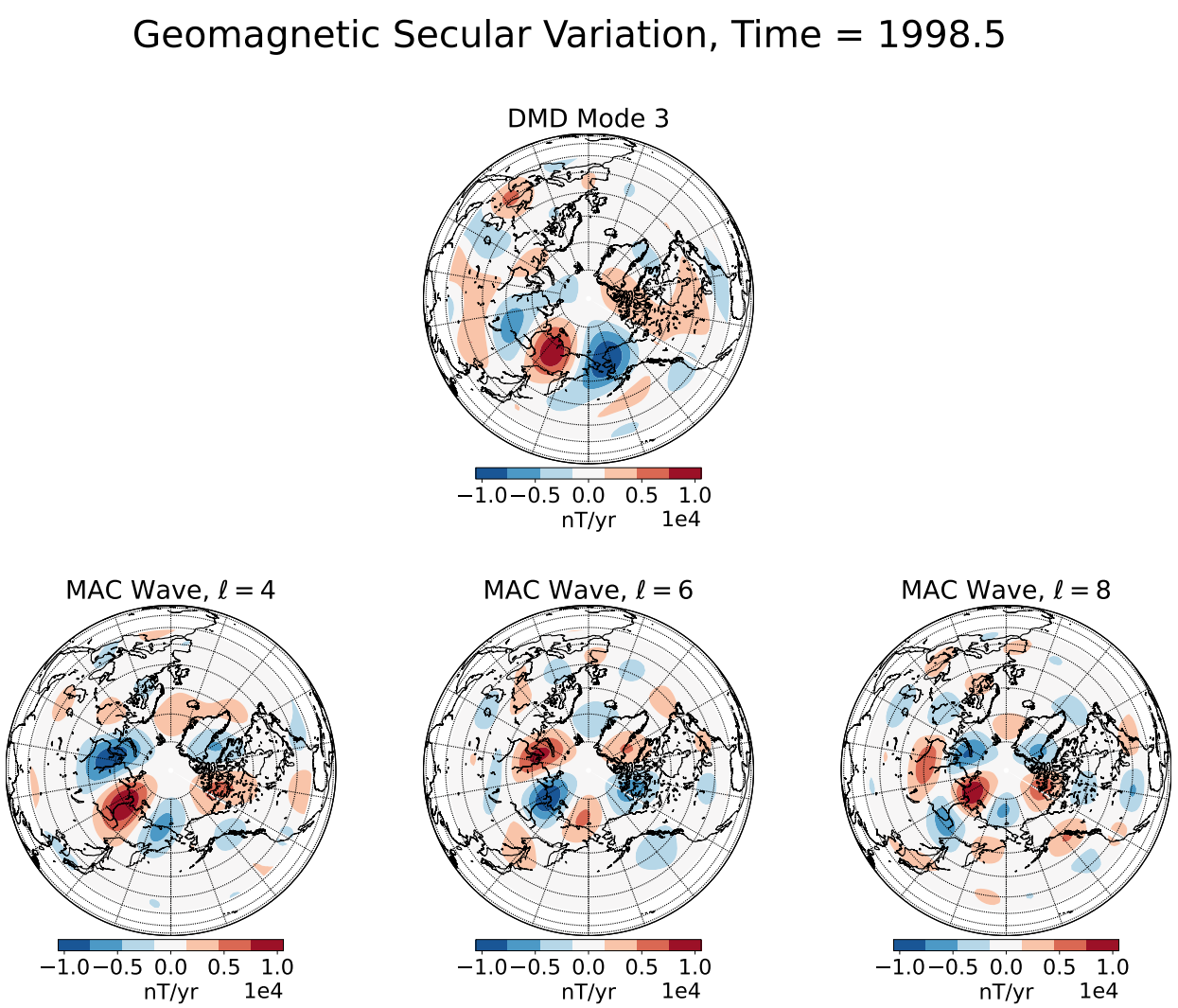

Figure 5.5: Comparison of DMD mode 3 and with predictions for three zonal MAC waves, identified by the dominant spherical harmonic degree $\ell = 4$, $\ell = 6$ and $\ell = 8$. All comparisons are made at $t = 1998.5$.

attributed to a zonal MAC wave with higher ℓ. To explore this possibility we adopt a 140-km layer with a peak buoyancy frequency of $N = 0.86\Omega$. Our prediction for $\ell = 12$ wave gives a period of 18.9 years and a quality factor of 4.6. While the period is in reasonable agreement, the quality factor is lower than $Q = 11.0$ for Modes 4 and 5. In addition, the spatial complexity of the predicted secular variation for an $\ell = 12$ wave is not compatible with the structure of Modes 4 and 5. (Note that the spatial structure of the secular variation depends on the wave structure and the distribution of radial magnetic field). Predictions for an $\ell = 8$ wave in Fig. 5.5 are already too complicated compared to the spatial structure

of Modes 4 and 5 in Fig. 5.1. Increasing the degree to $\ell = 12$ to match the period only makes the comparison of the spatial structure worse. We conclude that the predicted spatial patterns of higher ℓ MAC waves are not compatible with the spatial structure of Modes 4 and 5. Other types of waves should be explored to identify the origin of Modes 4 and 5. Alternatively, the geomagnetic signal may be a consequence of flow associated with the tangent cylinder (Livermore et al., 2017).

Our calculation of DMD modes depends on the number of singular values we use to construct the optimal dynamics matrix A. This choice determines the number of DMD modes that are recovered from the data. Since the DMD modes are not orthogonal we can expect a change in the spatial structure of the individual modes as the number of singular values are increased. Even though the overall fit to the observations should improve as the number singular values increases, our ability to interpret the individual modes could be compromised if these modes change when we retain too many singular values.

There are several ways to make an objective choice for the number of singular values. In this study we have followed the approach advocated by Brunton and Kutz (2019). This method sets a target for the cumulative variance (or energy) recovered from the original data by a limited number of singular values. In Fig. B.2, we plot the cumulative variance as a function of the number of singular values. Setting the threshold at 99.5% of the total variance limits the reconstruction to the first 5 modes. Contributions from individual modes above this threshold do little to improve the fit to the data.

Finally, we comment on the recovery of DMD modes with periods that exceed the duration of the record. We recall that the DMD method finds the optimal dynamics matrix $\tilde{A}$. In principle, a long-period oscillation could be recovered from a short record if the underlying dynamics is linear. Practical limitations arise in the presence of noise or when the dynamics is nonlinear. One way to test the recovery of long-period modes is to repeat the analysis on a longer record. For example, we consider a 30-year record of radial magnetic field and secular variation between 1988 and 2018 from the COV-OBSx2 model (Huder et al., 2020). We confine our attention to the northern hemisphere (as before) and retrieve 6 DMD modes from the longer record. Two modes correspond to secular trends ($\omega = 0$). The other four modes correspond to a pair of waves with periods of 51 years and 19.6 years. The amplitude of the 51-year mode is slightly smaller than the corresponding 60-year mode recovered from CHAOS-7 but the spatial structure of the mode is remarkably similar to that from CHAOS-7 (see Figure B.3).

Extending the COV-OBSx2 record to 55 years (1963 to 2018) has very little influence on the spatial structure of the 60-year DMD modes (see Figure S3), although the period increases to 74 years. While a longer record should improve the reliability of the recovered period, there is also a greater chance that stochastic generation of the wave by convection in the core will alter the temporal coherence. Broadly similar results from the shorter CHAOS-7

record is encouraging because we might try to average modes from short records to reduce the contribution of the generation process.

5.5 Conclusions

We apply the DMD technique to geomagnetic observations to quantify waves in the core. By combining observations of the geomagnetic field and secular variation we obtain an optimal description of the time variations in B_r and $\dot{B}_r$, corresponding to equations for secular variation and secular acceleration of the field. This is a powerful approach because no priori physical knowledge is needed to construct the modes. We simply look for patterns of spatial and temporal coherence in the observations. The DMD methodology opens a new way to study the time dependence of geomagnetic data and extract information about waves in the core.

The DMD modes recovered from the simultaneous analysis of B_r and $\dot{B}_r$ are compatible with the existence of two waves. One with a nominal period of 20 years and another with a nominal period of 60 years. Both of these waves had been reported in previous studies (Buffett et al., 2016; Chi-Durán et al., 2020). The advantage of the DMD method is that we recover estimates of the spatial structure and the frequency of the waves, including the damping time. The nominal 60-year wave is compatible with the structure and frequency of a zonal MAC wave, which requires fluid stratification at the top of the core. The shorter period wave does not appear to be due to a higher frequency (zonal) MAC wave. Other physical processes may contribute to origin of the 20-year variations.

Chapter 6

Conclusions and Future Work

Two data-driven techniques were successfully applied to geomagnetic observations to recover quantitative information about waves in the Earth's core. My analysis was restricted to the satellite era because the resulting improvements in the data quality enable reliable estimates for the second time derivative of the geomagnetic field (secular acceleration). I focus primarily on secular acceleration of the geomagnetic field to emphasize the role of waves in the core.

Chapter 3 applies the method of complex empirical orthogonal functions (CEOFs) to the CHAOS-6 model of geomagnetic secular acceleration. Several local regions with active secular acceleration were chosen for analysis. In each of the selected regions a large fraction of the observed variability was recovered with the first two CEOF modes. Evidence for eastward travelling waves was recovered from the region below Southeast Asia. Westward waves were recovered from the regions below Alaska and below the equatorial Atlantic.

An interpretation of the wave motion at high latitudes is presented in Chapter 4. Two candidate waves are proposed to match the observed period and phase velocity. The first candidate wave is a magnetic Rossby wave. This wave could account for the phase velocity, based on previously estimates for fluid stratification at the top of the core. However, the spatial complexity of the predicted secular acceleration was not compatible with the observations. An alternative interpretation involved zonal MAC waves. In this case the fluid motion due to the wave is purely zonal, so the longitudinal variation in the predicted secular acceleration is caused by longitudinal variations in the main field B_r. Westward and eastward propagation of the secular acceleration is predicted for this wave over a full cycle or period. Westward propagation from the CEOF modes should eventually give way to an eastward propagation of the next 5 years. This is a testable prediction of the second proposed wave.

Chapter 5 illustrates the utility of dynamic mode decomposition (DMD) for analyzing geomagnetic variations. This method was applied to both the secular variation and secular acceleration from the CHAOS-7 model. I identified waves with 20- and 60-year periods at high latitudes. The 20-year wave was remarkably similar to the CEOF mode reported below

Alaska in Chapter 3; the 60-year wave had been previously reported in studies of ground-based observations. An advantage of the DMD method is that it directly recovers both the frequency and the damping of the wave which is quantified in terms of a quality factor Q . The damping is a useful additional diagnostic for assessing the origin of these waves. The recovery a 60-year mode in twenty years of satellite data was a surprise. This detection was investigated using a longer data record that relied on ground-based observation prior to the satellite era. A very similar DMD mode was recovered from the longer data record. While the spatial pattern of the DMD was nearly invariant, the period increased slightly to about 70 years.

The CEOF and DMD methods are effective for identifying short-period waves without relying on a priori physical knowledge of outer core dynamics. Overall, data-driven techniques are efficient tools for detecting waves in geomagnetic data because they effectively filter the signals in space and time. As a result, it is possible to recover more reliable estimates of the wave properties. This is an important starting point identifying and interpreting the waves.

The stratified layer at the top of the core plays a crucial role in the behavior of waves observed in this thesis. Both magnetic Rossby and zonal MAC waves, which account for the geomagnetic acceleration at high latitudes, require the presence of a stratified layer. This stratification is characterized by buoyancy frequencies comparable to the rotation rate, indicative of thermal stratification. A stratified layer with appropriate thickness and strength may be responsible for the formation and propagation of waves observed using DMD and CEOF.

Future research entails further investigation of the relationship between CEOF and DMD. The DMD analysis could be expanded to encompass the entire equatorial region using time series of B_r and $\dot{B}_r$. Examining the consistency of the two techniques, which attempt to model common underlying dynamics in the CHAOS models, would be valuable. A notable advantage of the DMD method is its ability to recover localized dynamics even when applied to a more extensive region (e.g., the entire equatorial region). Such experiments may underscore the potential of DMD as a tool for identifying traveling magnetic waves in the core and offer supplementary insights into CEOFs. Additionally, other DMD parameters, such as the number of modes and power threshold decisions, need to be put on a firmer theoretical foundation.

In conclusion, this work provides a deeper understanding of Earth's core dynamics and offers novel approaches to studying time-dependent geomagnetic data. The results have the potential to be further tested and refined in the coming years, ultimately enhancing our knowledge of Earth's core processes.

Bibliography

Alfvén, H. (1943). On the existence of electromagnetic-hydromagnetic waves. *Arkiv. Mat. Astron. Fys.*

Aubert, J., & Finlay, C. C. (2019). Geomagnetic jerks and rapid hydromagnetic waves focusing at Earth's core surface. *Nat. Geosci.*, *12*(5), 393–398. https://doi.org/https://doi.org/10.1038/s41561-019-0355-1

Aubert, J., & Gillet, N. (2021). The interplay of fast waves and slow convection in geodynamo simulations nearing Earth's core conditions. *Geophys. J. Int.*, *225*(3), 1854–1873. https://doi.org/https://doi.org/10.1093/gji/ggab054

Backus, G., George, B., Parker, R. L., Parker, R., & Constable, C. (1996). *Foundations of geomagnetism*. Cambridge University Press.

Barnett, T. (1983). Interaction of the monsoon and Pacific trade wind system at interannual time scales part I: The equatorial zone. *Monthly Weather Review*, *111*(4), 756–773.

Barrois, O., Hammer, M. D., Finlay, C. C., Martin, Y., & Gillet, N. (2018). Assimilation of ground and satellite magnetic measurements: Inference of core surface magnetic and velocity field changes. *Geophys. J. Int.*, *215*(1), 695–712.

Bloxham, J., & Jackson, A. (1992). Time-dependent mapping of the magnetic field at the core-mantle boundary. *Journal of Geophysical Research: Solid Earth*, *97*(B13), 19537–19563.

Braginsky, S. I. (1970). Torsional magnetohydrodynamic vibrations in the earth's core and variations in day length. *Geomagnetism and Aeronomy*, *10*, 1.

Braginsky, S. I. (1993). MAC-Oscillations of the hidden ocean of the core. *J. Geomag. and Geoelect.*, *45*(11), 1517–1538. https://doi.org/https://doi.org/10.5636/jgg.45.1517

Braginsky, S. I. (1998a). Magnetic rossby waves in the stratified ocean of the core, and topographic core-mantle coupling. *Earth, planets and space*, *50*(8), 641–649.

Braginsky, S. I. (1998b). Magnetic Rossby waves in the stratified ocean of the core, and topographic core-mantle coupling. *Earth Planets Space*, *50*(8), 641–649. https://doi.org/https://doi.org/10.1186/BF03352159

Braginsky, S. I. (1999). Dynamics of the stably stratified ocean at the top of the core. *Physics of the earth and planetary interiors*, *111*(1-2), 21–34.

Brunton, S. L., & Kutz, J. N. (2019). *Data-driven science and engineering: Machine learning, dynamical systems, and control*. Cambridge University Press. https://doi.org/10.1017/9781108380690

Buffett, B., & Knezek, N. (2018). Stochastic generation of MAC waves and implications for convection in earth's core. *Geophys. J. Int.*, *212*(3), 1523–1535. https://doi.org/https://doi.org/10.1093/gji/ggx492

Buffett, B., Knezek, N., & Holme, R. (2016). Evidence for MAC waves at the top of earth's core and implications for variations in length of day. *Geophys. J. Int.*, *204*(3), 1789–1800. https://doi.org/https://doi.org/10.1093/gji/ggv552

Buffett, B., & Matsui, H. (2019). Equatorially trapped waves in Earth's core. *Geophys. J. Int.*, *218*(2), 1210–1225. https://doi.org/https://doi.org/10.1093/gji/ggz233

Canet, E., Finlay, C. C., & Fournier, A. (2014). Hydromagnetic quasi-geostrophic modes in rapidly rotating planetary cores. *Physics of the Earth and Planetary Interiors*, *229*, 1–15.

Chi-Durán, R., Avery, M. S., & Buffett, B. A. (2021). Signatures of high-latitude waves in observations of geomagnetic acceleration. *Geophys. Res. Lett.*

Chi-Durán, R., Avery, M. S., Knezek, N., & Buffett, B. A. (2020). Decomposition of geomagnetic secular acceleration into traveling waves using complex empirical orthogonal functions. *Geophys. Res. Lett.*, *47*(17). https://doi.org/https://doi.org/10.1029/2020GL087940

Chulliat, A., Alken, P., & Maus, S. (2015). Fast equatorial waves propagating at the top of the Earth's core. *Geophys. Res. Lett.*, *42*, 3321–3329. https://doi.org/https://doi.org/10.1002/2015GL064067

Chulliat, A., & Maus, S. (2014). Geomagnetic secular acceleration, jerks, and a localized standing wave at the core surface from 2000 to 2010. *J. Geophys. Res. [Solid Earth]*.

Chulliat, A., Thébault, E., & Hulot, G. (2010). Core field acceleration pulse as a common cause of the 2003 and 2007 geomagnetic jerks. *Geophysical Research Letters*, *37*(7).

Constable, C., & Johnson, C. (2005). A paleomagnetic power spectrum. *Physics of the Earth and Planetary Interiors*, *153*(1-3), 61–73.

De Boor, C. (1978). *A practical guide to splines* (Vol. 27). springer-verlag New York.

Domingos, J., Pais, M. A., Jault, D., & Mandea, M. (2019). Temporal resolution of internal magnetic field modes from satellite data. *Earth, Planets and Space*, *71*(1), 1–17.

Dumberry, M., & Finlay, C. C. (2007). Eastward and westward drift of the earth's magnetic field for the last three millennia. *Earth Planet. Sci. Lett.*, *254*(1), 146–157. https://doi.org/https://doi.org/10.1016/j.epsl.2006.11.026

Edwards, C. R., & Seim, H. E. (2008). Complex EOF analysis as a method to separate barotropic and baroclinic velocity structure in shallow water. *Journal of Atmospheric and Oceanic Technology*, *25*(5), 808–821.

Esquivel, P., & Messina, A. (2008). Complex empirical orthogonal function analysis of wide-area system dynamics. *2008 IEEE Power and Energy Society General Meeting-Conversion and Delivery of Electrical Energy in the 21st Century*, 1–7.

Finlay, C. C. (2019). Models of the main geomagnetic field based on multi-satellite magnetic data. *Ionospheric Multi-Spacecraft Analysis Tools: Approaches for Deriving Ionospheric Parameters*, *17*, 255.

Finlay, C. C., & Jackson, A. (2003). Equatorially dominated magnetic field change at the surface of earth's core. *Science*, *300*(5628), 2084–2086.

Finlay, C. C., Kloss, C., Olsen, N., Hammer, M. D., Tøffner-Clausen, L., Grayver, A., & Kuvshinov, A. (2020). The CHAOS-7 geomagnetic field model and observed changes in the South Atlantic anomaly. *Earth Planets Space*, *72*(1), 156. https://doi.org/https://doi.org/10.1186/s40623-020-01252-9

Finlay, C. C., Olsen, N., Kotsiaros, S., Gillet, N., & Tøffner-Clausen, L. (2016). Recent geomagnetic secular variation from swarm and ground observatories as estimated in the CHAOS-6 geomagnetic field model. *Earth Planets Space*, *68*(1), 112.

Finlay, C. C., Olsen, N., & Tøffner-Clausen, L. (2015). DTU candidate field models for IGRF-12 and the CHAOS-5 geomagnetic field model. *Earth, Planets and Space*, *67*(1), 114.

Fournier, A., Aubert, J., Lesur, V., & Ropp, G. (2021). A secular variation candidate model for IGRF-13 based on swarm data and ensemble inverse geodynamo modelling. *Earth Planets Space*, *73*(1), 43. https://doi.org/https://doi.org/10.1186/s40623-020-01309-9

Friis-Christensen, E., Lühr, H., & Hulot, G. (2006). Swarm: A constellation to study the earth's magnetic field. *Earth Planets Space*, *58*(4), 351–358.

Gerick, F., Jault, D., & Noir, J. (2021). Fast quasi-geostrophic magneto-coriolis modes in the earth's core. *Geophys. Res. Lett.*, *48*, e2020GL090803.

Gillet, N., Gerick, F., Angappan, R., & Jault, D. (2022). A dynamical prospective on interannual geomagnetic field changes. *Surveys in Geophysics*, *43*(1), 71–105.

Gillet, N., Huder, L., & Aubert, J. (2019). A reduced stochastic model of core surface dynamics based on geodynamo simulations. *Geophys. J. Int.*, *219*, 522–539.

Gillet, N., Jault, D., Finlay, C. C., & Olsen, N. (2013). Stochastic modeling of the earth's magnetic field: Inversion for covariances over the observatory era. *Geochem. Geophys. Geosyst.*, *14*(4), 766–786.

Gubbins, D., & Davies, C. (2013). The stratified layer at the core–mantle boundary caused by barodiffusion of oxygen, sulphur and silicon. *Physics of the Earth and Planetary Interiors*, *215*, 21–28.

Hammer, M. D., Cox, G. A., Brown, W. J., Beggan, C. D., & Finlay, C. C. (2021). Geomagnetic virtual observatories: Monitoring geomagnetic secular variation with the swarm satellites. *Earth, Planets and Space*, *73*(1), 1–22.

Hardy, C., Livermore, P., & Niesen, J. (2020). Enhanced magnetic fields within a stratified layer. *Geophys. J. Int.*, *222*, 1686–1702.

Hide, R. (1966). Free hydromagnetic oscillations of the earth's core and the theory of the geomagnetic secular variation. *Philosophical Transactions of the Royal Society of London. Series A, Mathematical and Physical Sciences*, *259*(1107), 615–647.

Holme, Olson, & Schubert. (2015). Large-scale flow in the core. *Treatise on geophysics*.

Holme, R. (2007). 8.04-large-scale flow in the core. *Treatise on Geophysics, edited by Olsen, P. and Schubert, G*, 107–130.

Holme, R. (2015). Large-scale flow in the core. In *Treatise on geophysics* (pp. 91–113). Elsevier. https://doi.org/https://doi.org/10.1016/B978-0-444-53802-4.00138-X

Horel, J. D. (1984). Complex principal component analysis: Theory and examples. *Journal of climate and Applied Meteorology*, *23*(12), 1660–1673.

Hori, K., Jones, C., & Teed, R. (2015). Slow magnetic rossby waves in the earth's core. *Geophysical Research Letters*, *42*, 6622–6629.

Huder, L., Gillet, N., Finlay, C. C., Hammer, M. D., & Tchoungui, H. (2020). COV-OBS.x2: 180 years of geomagnetic field evolution from ground-based and satellite observations. *Earth, Planets, Space*, *72*, 160. https://doi.org/https://doi.org/10.1186/s40623-020-01194-2

Jackson, A., & Finlay, C. (2015). Geomagnetic secular variation and its applications to the core. In G. Schubert (Ed.), *Treatise on geophysics* (2nd ed., pp. 137–184). Elsevier.

Jackson, A., Jonkers, A. R. T., & Walker, M. R. (2000). Four centuries of geomagnetic secular variation from historical records. *Philosophical Transactions of the Royal Society of London. Series A: Mathematical, Physical and Engineering Sciences*, *358*(1768), 957–990.

Knezek, N., & Buffett, B. (2018). Influence of magnetic field configuration on magnetohydrodynamic waves in earth's core. *Physics of the Earth and Planetary Interiors*, *277*, 1–9.

Koot, L., Dumberry, M., Rivoldini, A., DeViron, O., & Dehant, V. (2010). Constraints on coupling at the core-mantle and inner-core boundaries inferred from observations of nutations. *Geophys. J. Int.*, *182*, 1279–1294.

Korte, M., Constable, C., Donadini, F., & Holme, R. (2011). Reconstructing the Holocene geomagnetic field. *Earth Planet. Sci. Lett.*, *312*(3), 497–505. https://doi.org/https://doi.org/10.1038/ngeo2859

Lehnert, B. (1954). Magnetohydrodynamic waves under the action of the coriolis force. *Astrophysical Journal, vol. 119, p. 647*, *119*, 647.

Lehoucq, R. B., Sorensen, D. C., & Yang, C. (1998). *Arpack users' guide: Solution of large-scale eigenvalue problems with implicitly restarted arnoldi methods*. SIAM.

Lesur, V., Gillet, N., Hammer, M., & Mandea, M. (2022). Rapid variations of earth's core magnetic field. *Surveys in Geophysics*, *43*(1), 41–69.

Lesur, V., Wardinski, I., Hamoudi, M., & Rother, M. (2010). The second generation of the GFZ reference internal magnetic model: GRIMM-2. *Earth Planets Space*, *62*(10), 6. https://doi.org/https://doi.org/10.5047/eps.2010.07.007

Livermore, P. W., Hollerbach, R., & Finlay, C. C. (2017). An accelerating high-latitude jet in earth's core. *Nat. Geosci.*, *10*(1), 62–68. https://doi.org/https://doi.org/10.1038/ngeo2859

Matzka, J., Chulliat, A., Mandea, M., Finlay, C. C., & Qamili, E. (2010). Geomagnetic observations for main field studies: From ground to space. *Space Science Reviews*, *155*, 29–64.

Maus, S. (2007). Champ. In D. Gubbins & H. Herrero-Bervera (Eds.), *Encyclopedia of geomagnetism and paleomagnetism* (pp. 59–60). Springer.

Maze, G. (2020). PCAtool. In *Www.mathworks.com/matlabcentral/fileexchange* (p. 17915). MATLAB Central File Exchange.

Olsen, N., Albini, G., Bouffard, J., Parrinello, T., & Tøffner-Clausen, L. (2020). Magnetic observations from cryosat-2: Calibration and processing of satellite platform magnetometer data. *Earth, Planets and Space*, *72*, 1–18.

Olsen, N., Lühr, H., Finlay, C. C., Sabaka, T. J., Michaelis, I., Rauberg, J., & Tøffner-Clausen, L. (2014). The CHAOS-4 geomagnetic field model. *Geophysical Journal International*, *197*(2), 815–827.

Olsen, N., Lühr, H., Sabaka, T. J., Mandea, M., Rother, M., Tøffner-Clausen, L., & Choi, S. (2006). CHAOS—a model of the earth's magnetic field derived from CHAMP, Ørsted, and SAC-C magnetic satellite data. *Geophys. J. Int.*, *166*(1), 67–75.

Olsen, N., & Mandea, M. (2008). Rapidly changing flows in the Earth's core. *Nat. Geosci.*, *1*(6), 390–394. https://doi.org/https://doi.org/10.1007/s12110-009-9068-2

Olsen, N., Mandea, M., Sabaka, T. J., & Tøffner-Clausen, L. (2009). CHAOS-2—a geomagnetic field model derived from one decade of continuous satellite data. *Geophysical Journal International*, *179*(3), 1477–1487.

Olsen, N., Mandea, M., Sabaka, T. J., & Tøffner-Clausen, L. (2010). The CHAOS-3 geomagnetic field model and candidates for the 11th generation IGRF. *Earth, Planets and Space*, *62*(10), 1.

Olsen, N., & Stolle, C. (2012). Satellite geomagnetism. *Annual Review of Earth and Planetary Sciences*, *40*, 441–465.

Pais, M., Alberto, P., & Pinheiro, F. (2015). Time-correlated patterns from spherical harmonic expansions: Application to geomagnetism. *Journal of Geophysical Research - Solid Earth*, *120*, 8012–8030.

Perko, L. (2013). *Differential equations and dynamical systems*. Springer Science & Business Media.

Pick, L., Korte, M., Thomas, Y., Krivova, N., & Wu, C.-J. (2019). Evolution of large-scale magnetic fields from near-earth space during the last 11 solar cycles. *Journal of Geophysical Research: Space Physics*, *124*(4), 2527–2540.

Roberts, P. H., Yu, Z. J., & Russell, C. T. (2007). On the 60-year signal from the core. *Geophys. Astrophys. Fluid Dyn.*, *101*, 11–35. https://doi.org/https://doi.org/10.1080/03091920601083820

Ropp, G., Lesur, V., Baerenzung, J., & Holschneider, M. (2020). Sequential modeling of the earth's core magnetic field. *Earth,Planets and Space*, *72*, 153.

Rowley, C. W., Mezić, I., Bagheri, S., Schlatter, P., & Henningson, D. S. (2009). Spectral analysis of nonlinear flows. *J. Fluid Mech.*, *641*, 115–127.

Sabaka, T. J., Olsen, N., Tyler, R. H., & Kuvshinov, A. (2015). CM5, a pre-swarm comprehensive geomagnetic field model derived from over 12 yr of CHAMP, Ørsted, SAC-C and observatory data. *Geophysical Journal International*, *200*(3), 1596–1626.

Schmid, P. J. (2010). Dynamic mode decomposition of numerical and experimental data. *Journal of Fluid Mechanics*, *656*, 5–28. https://doi.org/10.1017/S0022112010001217

Schmid, P. J. (2011). Application of the dynamic mode decomposition to experimental data. *Exp. Fluids*, *50*(4), 1123–1130.

Schmid, P. J. (2022). Dynamic mode decomposition and its variants. *Annu. Rev. Fluid Mech.*, *54*(1), 225–254.

Susanto, R. D., Zheng, Q., & Yan, X.-H. (1998). Complex singular value decomposition analysis of equatorial waves in the Pacific observed by TOPEX/Poseidon altimeter. *Journal of Atmospheric and Oceanic Technology*, *15*(3), 764–774.

Tilgner, A. (2015). Rotational dynamics of the core. In G. Schubert (Ed.), *Treatise on geophysics* (2nd ed., pp. 183–212). Elsevier.

Tu, J. H., Rowley, C. W., Luchtenburg, D. M., Brunton, S. L., & Nathan Kutz, J. (2014). On dynamic mode decomposition: Theory and applications. *Journal of Computational Dynamics*, *1*(2), 391–421.

Yokoyama, Y., & Yukutake, T. (1991). Sixty year variation in a time series of geomagnetic gauss coefficients between 1910 and 1983. *J. Geomagn. Geoelect.*, *43*, 563–584. https://doi.org/https://doi.org/10.5636/jgg.43.563

Appendix A

Supplementary Materials of Signatures of High-Latitude Waves in Observations of Geomagnetic Acceleration

This supplementary material has been previously published in Chi-Durán, R., Avery, M. S., & Buffett, B. A. (2021). *Signatures of high-latitude waves in observations of geomagnetic acceleration.* Geophysical Research Letters, 48, e2021GL094692. https://doi.org/10.1029/2021GL094692

A.1 Introduction

The supporting information includes the description of the methods used for modelling the high-latitudes waves in the geomagnetic acceleration. We also include a Figure (A.1) showing the predicted geomagnetic acceleration near the South Pole and a series of Snapshots (A.1) which provides an animation of the temporal evolution of CHAOS7, Magnetic Rossby waves and Zonal MAC waves.

A.2 Description of the models

CHAOS7 Model

We use the CHAOS7 model (Finlay et al., 2020) (version 7.6) to quantify the contribution of high-latitude waves. The field model is represented using a spherical harmonic expansion with time dependent Gauss coefficients. The time dependence is expressed in terms of B-splines so that first- and second-order derivatives in B_r can be computed with high accuracy. We compare the field model with predictions for $\dot{B}_r$ and $\ddot{B}_r$ using a prescribed wave velocity

v_ϕ and acceleration $\dot{v}_\phi$. These predictions for $\dot{B}_r$ and $\ddot{B}_r$ are computed using finite differences on a geographic grid with 100 grid points in latitude and 200 grid points in longitude.

Description of Magnetic Rossby Waves

Wave velocities and accelerations are computed using previously published models (Buffett & Knezek, 2018; Buffett & Matsui, 2019). A global model for magnetic Rossby waves in a spherical geometry is based on equation (37) of Buffett and Matsui (2019). This equation retains a full description of the spherical geometry but introduces the simplifying approximation of a constant rms radial magnetic field. The standard beta-plane and extended beta-plane approximations in Buffet and Matsui (2019) represent simplifications of equation (37) for the case of eastward propagating equatorial MAC waves. A direct numerical solution of equation (37) would give equatorial MAC waves without the beta-plane approximation. The same governing equation also describes westward-propagating high-latitude magnetic Rossby waves. We discretize equation (37) using finite differences and solve the linear system of equations as an eigenvalue problem using ARPACK (Lehoucq et al., 1998). The basic physical model assumes a constant buoyancy frequency across the layer.

Description of Zonal MAC Waves

Zonal MAC waves are computed numerically using the approach described in Buffett and Knezek (2018). In that study a wave equation was derived for the ϕ component of the magnetic perturbation (see equation (18) in Buffett and Knezek (2018)). The unforced governing equation is discretized using finite differences and solved for the natural frequency of the waves. The velocity v_ϕ is reconstructed from the solution for the magnetic perturbation b_ϕ using the magnetic induction equation. The full influence of radial magnetic diffusion is retained in this calculation. Our specific formulation from Buffett and Knezek (2018) is flexible enough to allow depth dependence in the stratification and latitudinal variations in the rms radial magnetic field. We adopt a linear change in buoyancy frequency across the layer. We also allow the rms radial magnetic field to increase toward the poles. The form of the latitude dependence in this study is based on a recent high-resolution dynamo model (Buffett & Matsui, 2019).

A.3 Figure A.1

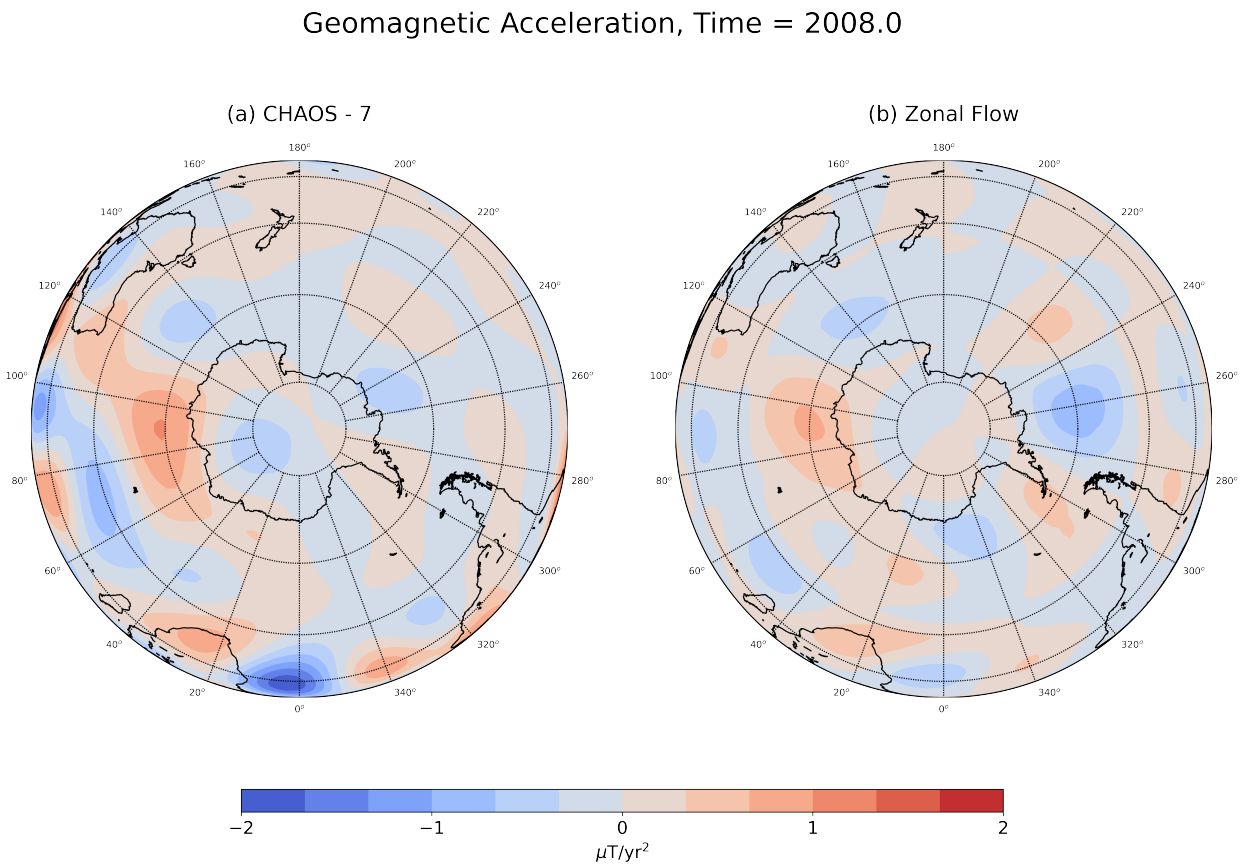

Figure A.1: South polar view of observed and predicted geomagnetic acceleration in 2008. Prediction is based on a purely zonal flow and acceleration. The overall amplitude is weaker in the southern hemisphere than the north. The amplitude of the prediction is due to weaker gradients in large scale B_r.

A.4 Captions for the Snapshots

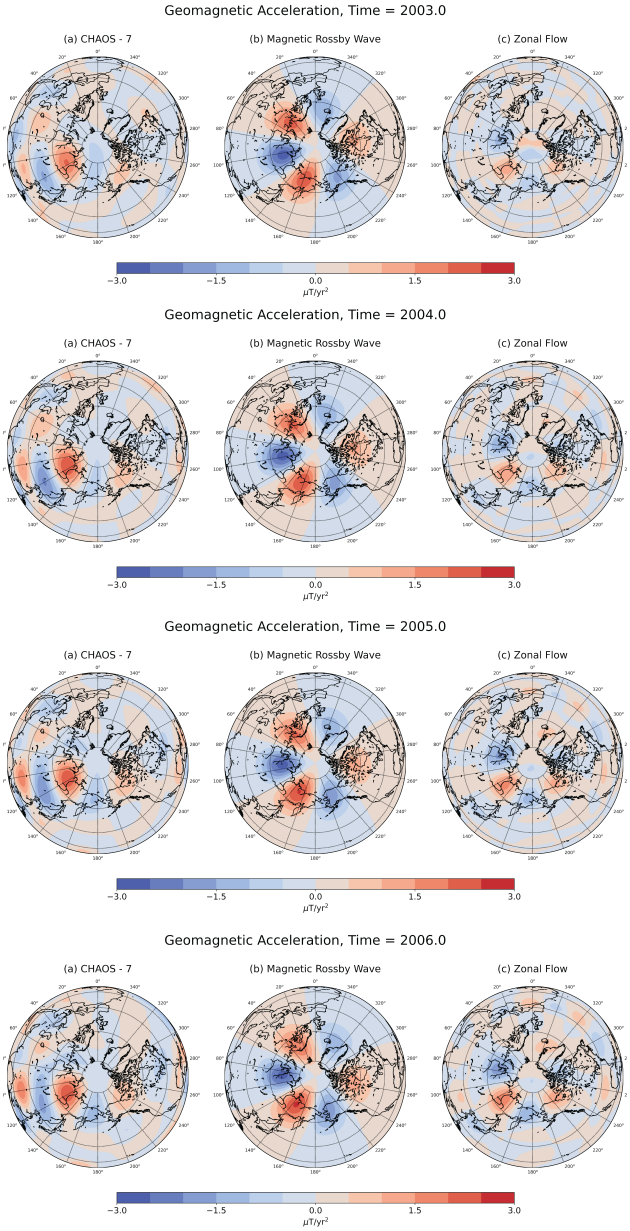

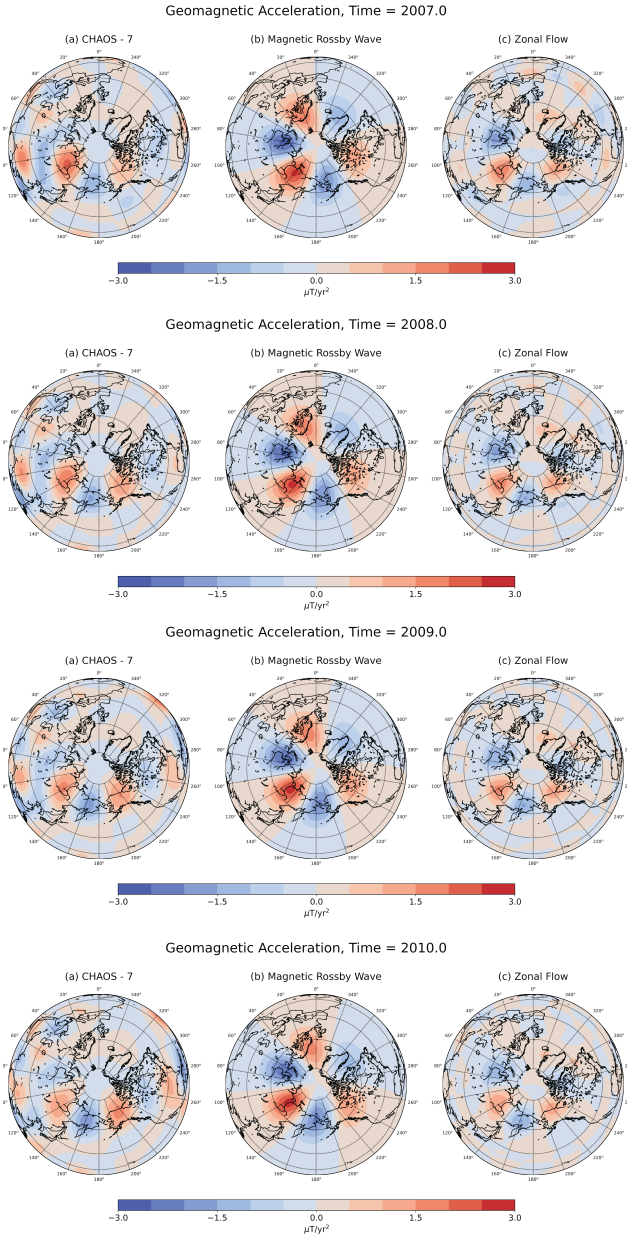

Snapshots of the temporal evolution of the geomagnetic acceleration between 2002 - 2010. (a) Geomagnetic acceleration from CHAOS7 model (Finlay et al., 2020). (b) $m = 3$ magnetic Rossby wave with $H = 132$ km and $N = 0.6\Omega$. (c) Zonal MAC wave represented using a purely zonal fluid flow. Pulses of secular acceleration are evident in all three panels between longitudes 90° to 240°.

Appendix B

Supplementary Materials of Decomposition of geomagnetic secular acceleration into traveling waves using complex empirical orthogonal functions

This supplementary material has been previously published in Chi-Durán, R., & Buffett, B. A. (2023). *Extracting spatial–temporal coherent patterns in geomagnetic secular variation using dynamic mode decomposition*. Geophysical Research Letters, 50, e2022GL101288. https://doi. org/10.1029/2022GL101288

B.1 Introduction

The supporting information includes three additional Figures which support the information provided in Chapter 5.

B.2 Figure B.1

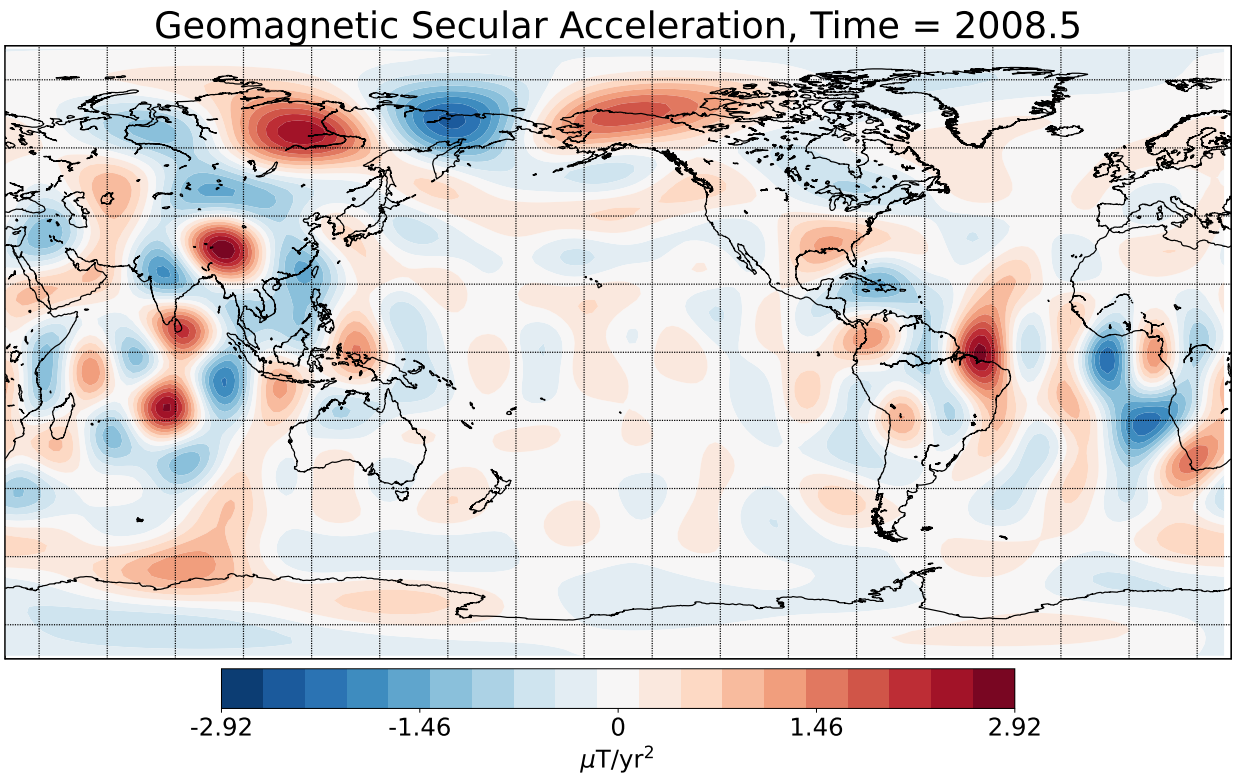

Figure B.1: Geomagnetic Secular Acceleration from CHAOS-7 model on 2008.5 from the CHAOS-7 model Finlay et al., 2020. High activity is identified in the North Pole (between Siberia and Alaska) and in the equatorial region (Southeast Asia and over the Atlantic ocean).

B.3 Figure B.2

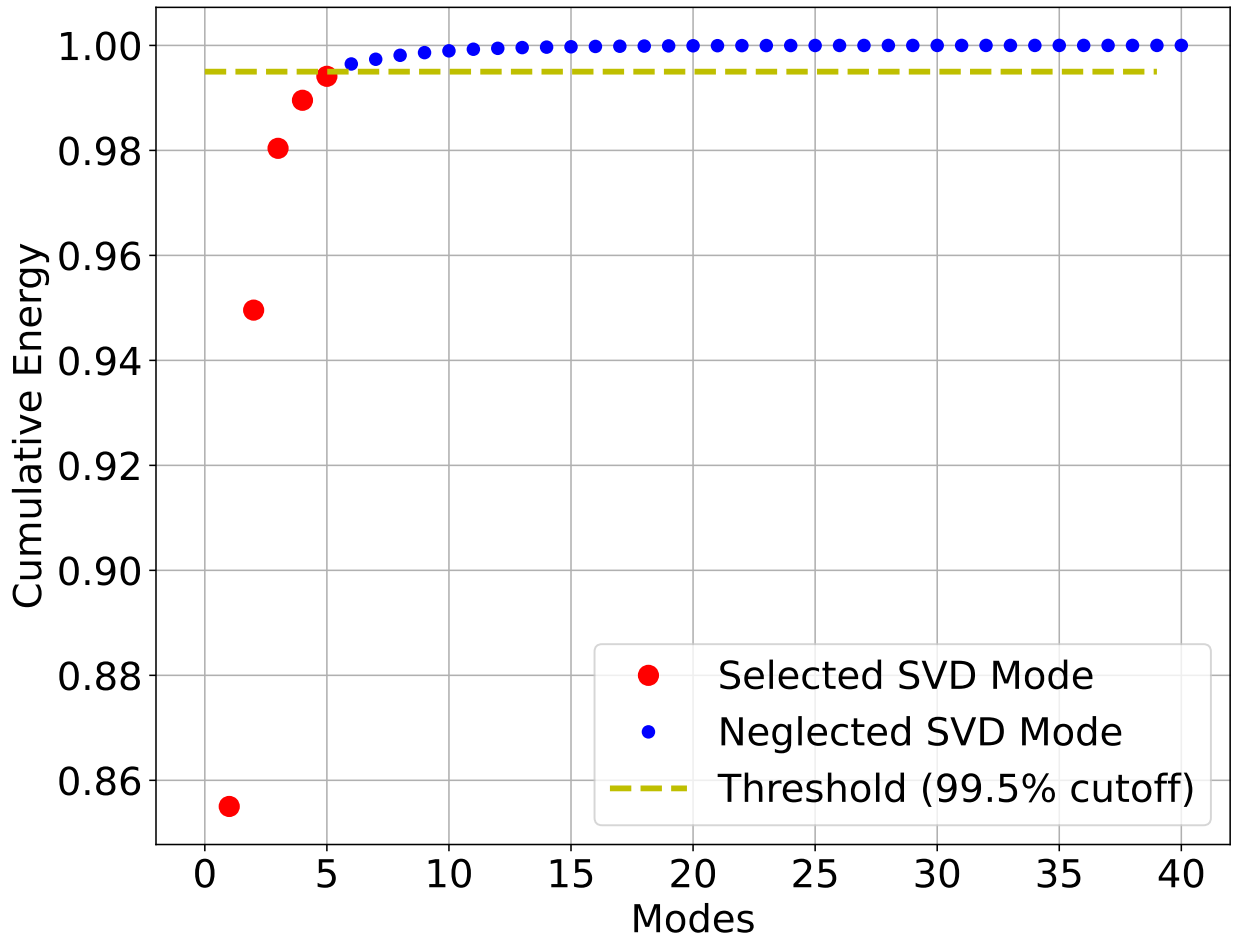

Figure B.2: Cumulative variance from the singular value decomposition of the input data. A larger number of singular values captures more of the variance in the data.

B.4 Figure B.3

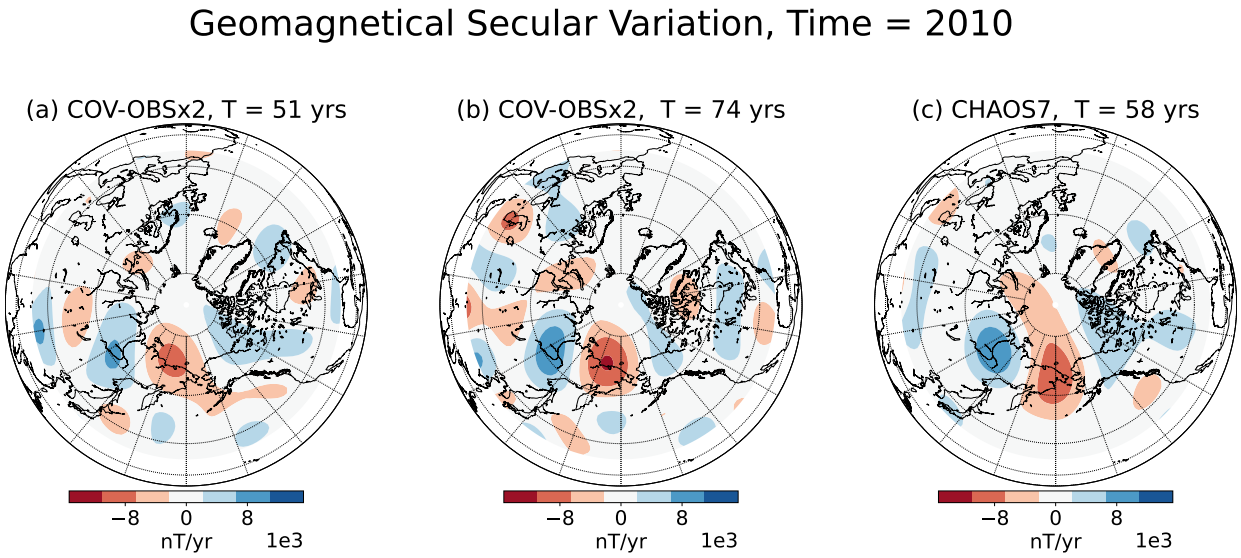

Figure B.3: (a) Spatial Structure and period of long-period mode in Geomagnetic Secular Variation at 2010 using 30-year record of COV-OBSx2 model (1987.5 to 2017.5) (b) Long-period mode in Geomagnetic Secular Variation at 2010 using 55-year record of COV-OBSx2 model (1962.5 and 2017.5) (c) Long-period mode in Geomagnetic Secular Variation at 2010 using 20-year record of CHAOS-7 model (1998.5 and 2018).